



A Stochastic Approach to Reconstruct Gamma-Ray-burst Light Curves

Maria G. Dainotti¹ , Ritwik Sharma² , Aditya Narendra^{3,4} , Delina Levine⁵ , Enrico Rinaldi⁶ , Agnieszka Pollo^{3,7} , and Gopal Bhatta⁸

¹ National Astronomical Observatory of Japan, 2 Chome-21-1 Osawa, Mitaka, Tokyo 181-8588, Japan

² Department of Physics, Deshbandhu College, University of Delhi, New Delhi, India

³ Astronomical Observatory of Jagiellonian University, Krakow, Poland

⁴ Jagiellonian University, Doctoral School of Exact and Natural Sciences, Krakow, Poland

⁵ Department of Astronomy, University of Maryland, College Park, MD 20742, USA

⁶ Interdisciplinary Theoretical & Mathematical Science Program, RIKEN (iTHEMS), 2-1 Hirosawa, Wako, Saitama 351-0198, Japan

⁷ National Centre for Nuclear Research, Warsaw, Poland

⁸ Institute of Nuclear Physics Polish Academy of Sciences, PL-31342 Krakow, Poland

Received 2023 January 13; revised 2023 May 18; accepted 2023 May 18; published 2023 August 8

Abstract

Gamma-ray bursts (GRBs), as they are observed at high redshift ($z=9.4$), are vital to cosmological studies and investigating Population III stars. To tackle these studies, we need correlations among relevant GRB variables with the requirement of small uncertainties on their variables. Thus, we must have good coverage of GRB light curves (LCs). However, gaps in the LC hinder the precise determination of GRB properties and are often unavoidable. Therefore, extensive categorization of GRB LCs remains a hurdle. We address LC gaps using a stochastic reconstruction, wherein we fit two preexisting models (the Willingale model; W07; and a broken power law; BPL) to the observed LC, then use the distribution of flux residuals from the original data to generate data to fill in the temporal gaps. We also demonstrate a model-independent LC reconstruction via Gaussian processes. At 10% noise, the uncertainty of the end time of the plateau, its correspondent flux, and the temporal decay index after the plateau decreases by 33.3%, 35.03%, and 43.32% on average for the W07, and by 33.3%, 30.78%, 43.9% for the BPL, respectively. The uncertainty of the slope of the plateau decreases by 14.76% in the BPL. After using the Gaussian process technique, we see similar trends of a decrease in uncertainty for all model parameters for both the W07 and BPL models. These improvements are essential for the application of GRBs as standard candles in cosmology, for the investigation of theoretical models, and for inferring the redshift of GRBs with future machine-learning analyses.

Unified Astronomy Thesaurus concepts: [Gamma-ray bursts \(629\)](#); [Gamma-rays \(637\)](#); [Gamma-ray astronomy \(628\)](#)

Supporting material: machine-readable tables

1. Introduction

Gamma-ray bursts (GRBs) are transient astrophysical events that can be observed up to redshift $z=8.2$ (Salvaterra et al. 2009; Tanvir et al. 2009) and $z=9.4$ (Cucchiara et al. 2011). Thus, they are excellent candidates for cosmological tools that can be used to probe the early Universe. Moreover, a comprehensive characterization of GRBs can provide insight into Population III stars, the most ancient stars observed at the epoch of reionization. Having a reliable taxonomy of GRB classes and good data coverage will favor future population studies and thus will enhance the determination of the cosmological evolution of GRB properties and the investigation of their emission mechanism and/or progenitors. All these are foundational topics for astrophysics.

The lack of a robust GRB classification scheme, the incompleteness of redshift information in the existing sample of observed GRBs, gaps in the light curves (LCs), and the need for a unique database repository are some of the many difficult challenges that astrophysicists need to overcome. In this paper, we attempt to solve the issue related to the temporal gaps in the LCs.

Observationally, GRB emission can be divided into two phases: the prompt, and the afterglow. The prompt is the primary phase observed from high-energy γ -rays to X-rays and sometimes in optical bands (Blake et al. 2005; Vestrand et al. 2005; Beskin et al. 2010; Gorbovskoy et al. 2012; Vestrand et al. 2014). The prompt is followed by an afterglow phase (Costa et al. 1997; van Paradijs et al. 1997; Piro et al. 1998; Gehrels et al. 2009) that is observed in multiple wavelengths such as X-rays, optical, and sometimes radio bands.

Historically, GRBs have been divided into two classes depending on their prompt duration, T_{90} , the time interval during which a burst releases 90% of its total background-subtracted counts, beginning after 5% of the total counts have been measured (Mazets et al. 1981; Kouveliotou et al. 1993). Short GRBs (SGRBs), with $T_{90} \leq 2$ s, are produced by the merging of compact objects (Duncan & Thompson 1992; Narayan et al. 1992; Usov 1992; Thompson 1994; Leván et al. 2008; Metzger et al. 2011; Bucciantini et al. 2012; Perna et al. 2016), and long GRBs (LGRBs), with $T_{90} \geq 2$ s, result from collapsing massive stars (Woosley 1993; Paczyński 1998; MacFadyen & Woosley 1999; Bloom et al. 2002; Hjorth et al. 2003; Woosley & Bloom 2006; Woosley & Heger 2006; Bucciantini et al. 2008; Kumar et al. 2008; Hjorth & Bloom 2012; Cano et al. 2017; Lyman et al. 2017; Perna et al. 2018; Ahumada et al. 2021; Aloy & Obergaulinger 2021). However, this historical classification into LGRBs and SGRBs simplifies a more complex and realistic picture where many



Original content from this work may be used under the terms of the [Creative Commons Attribution 4.0 licence](#). Any further distribution of this work must maintain attribution to the author(s) and the title of the work, journal citation and DOI.

more classes have been discovered in the literature since then (see Section 1.3 for more details). In the analysis proposed here, the reconstruction of GRB LCs will improve GRB characterization to cast further light on the different classes.

The Neil Gehrels Swift Observatory (Swift; Gehrels et al. 2004) is crucial for observing GRB temporal properties. The Swift Burst Alert Telescope (BAT, 15–150 keV; Barthelmy et al. 2005) enables the rapid detection of the prompt emission and a fast follow-up of the afterglow by the X-ray (XRT, 0.3–10 keV; Burrows et al. 2005) and ultraviolet telescopes (UVOT 170–600 nm; Roming et al. 2005). Furthermore, due to rapid afterglow follow-up in several wavelengths, Swift data have shown new features in the GRB LCs (Tagliaferri et al. 2005; Nousek et al. 2006; Troja et al. 2007).

Many X-ray LCs have a steep flux decay after the prompt emission ends, sometimes followed by flares and a plateau (Nousek et al. 2006; O’Brien et al. 2006; Zhang et al. 2006; Willingale et al. 2007; Liang et al. 2007; Sakamoto et al. 2007; Dainotti et al. 2008, 2010, 2016, 2017). Specifically, XRT detections are available for 81% of the Swift GRBs: 42% have X-ray plateaus (Evans et al. 2009; Li et al. 2018b). The X-ray plateau generally lasts 10^2 – 10^5 s and has a subsequent phase characterized by a power-law (PL) decay. In addition, about 30% of optical LCs observed by UVOT and ground-based facilities also exhibit a shallow decay phase (Vestrand et al. 2005; Kann et al. 2006; Zeh et al. 2006; Panaitescu & Vestrand 2008; Kann et al. 2010, 2011; Panaitescu & Vestrand 2011; Li et al. 2012; Oates et al. 2012; Margutti et al. 2013; Zaninoni et al. 2013; Melandri et al. 2014; Li et al. 2015, 2018a; Si et al. 2018; Dainotti et al. 2020b). The plateau can be fitted with a BPL (Zhang et al. 2006; Racusin et al. 2009), a smoothly broken PL (SBPL), or the Willingale et al. (2007) phenomenological model (W07; Willingale et al. 2007). The W07 model determines the time at the end of the plateau (T_a), its corresponding flux (F_a), and the temporal index after the plateau (α_a). The BPL determines T_a , F_a , and the slope of the LC during the plateau (α_1) and after the plateau (α_2). These models are briefly described in Section 2.1.

The plateau is usually explained via the magnetar model, based on the dipole radiation emitted by the rotational energy of a newly born neutron star (NS). In this model, the plateau ends when the NS reaches its critical spin-down timescale; the uncertainties on T_a can be ascribed to the uncertainties on the magnetar spin period and magnetic field.

However, the characterization of the plateau emission can be hindered by temporal gaps, which can occur in the beginning, during, and at the end of the plateau. These may arise from the orbital period of satellites, lack of fast follow-up studies, atmospheric turbulence, and instrumental errors or failures. Thus, the extensive characterization of GRB LCs remains a bottleneck.

Therefore, we propose a method for reconstructing LCs starting from the plateau emission, which, due to its theoretical interpretation within the magnetar model, is grounded in fundamental physics. Morphologically, the plateau has more standard features among diverse GRBs (e.g., its length and flatness) than the prompt properties. The plateau features have attracted attention due to their use in building relevant correlations with the plateau parameters and their application as cosmological tools. Specifically, Dainotti et al. (2008, 2010, 2011, 2013, 2015, 2017) and Li et al. (2018b) explored the luminosity at the end of the plateau, $L_{X,a}$, versus

its rest-frame time $T_{X,a}^*$ (known as the Dainotti relation, or 2D L-T relation).⁹ The 2D relation has also been discovered in optical plateau emissions (Dainotti et al. 2020b, 2022f). Within the theoretical magnetar scenario, Rowlinson et al. (2014) showed that the X-ray Dainotti relation is reproduced with a slope for $L_{a,X}T_{a,X}^*$ of -1 . This correlation has already been applied in the cosmological framework to construct a GRB Hubble diagram out to $z > 8$ (Cardone et al. 2009, 2010; Dainotti et al. 2013; Postnikov et al. 2014).

An extension of the 2D L-T relation, obtained by adding the peak prompt luminosity, $L_{X,\text{peak}}$, has led to the Dainotti 3D relation (Dainotti et al. 2016, 2017, 2020a, 2022f). This 3D relation has also been successfully applied to constrain cosmological parameters (Cao et al. 2022a, 2022b; Dainotti et al. 2022b, 2022d, 2022e, 2023b). Importantly, Dainotti et al. (2022d) have shown that if we reduce the uncertainties on the parameters of the plateau emission by 47.5%, we will reach the same precision on the cosmological value of Ω_M quoted in Conley et al. (2011) even now, compared to the same accuracy that we would reach in 2037 based on current observation rates and parameter uncertainties. This shows how appealing a more robust LC reconstruction (LCR) can be, given that it would save us 15 yr of observations to reduce the uncertainties on cosmological parameters to reach the same precision as achieved by supernovae (SNe) Ia (for details, see Dainotti et al. 2020a).

In addition, the plateau emission has been the object of investigation concerning the closure relations (the relations between the temporal and spectral index during or after the plateau region), which allows us to test the viability of the standard fireball model for the observations carrying plateau emission in high-energy γ -rays, X-rays, or optical wavelengths (Willingale et al. 2007; Evans et al. 2009; Racusin et al. 2009; Kumar & Barniol Duran 2010; Oates et al. 2012; Gao et al. 2013; Wang et al. 2015; Tak et al. 2019; Srinivasaragavan et al. 2020; Fraija et al. 2020; Ryan et al. 2020; Dainotti et al. 2021b, 2021d, 2022c, 2023a; Misra et al. 2021; Levine et al. 2023). Although closure relations are a quick way to test the standard fireball model, a more precise characterization of the decay index after the plateau emission would allow for better precision in determining these relations.

Finally, another relevant application is to use the reconstructed LCs to train machine-learning models for a redshift estimation and classification of all redshifts, especially of high- z GRBs.

Because of the many applications, both from a theoretical and a cosmological perspective, the plateau parameters must be well constrained. In this regard, reconstructing LCs with plateaus in the plateau region is extremely important. Indeed, LCs with gaps are in many circumstances not usable for cosmological applications. In addition, LCs with temporal gaps cannot be reliably used to test theoretical models that attempt to explain the GRB emission (e.g., the standard fireball model; Cavallo & Rees 1978; Meszaros & Rees 1993; Meszaros 1997; Piran 1999; Panaitescu & Kumar 2000; Mészáros 2001; Panaitescu & Kumar 2001; Zhang & Meszaros 2002; Piran 2004; Zhang & Mészáros 2004; Zhang et al. 2006; Scargle 2020). Thus, LCs with better coverage will facilitate the modeling and determining the correlations among critical physical properties.

⁹ The rest-frame time is denoted with an asterisk.

Our reconstruction method gives us a glimpse into what the data likely would have been in these gaps and increases the overall density distribution of the LCs over time. As a result, we can improve how well LCs can be used as standard candles and for theoretical modeling.

In this paper, we take the first step toward a full LCR: we develop a reconstruction technique and test its performance on our data set. This paper is divided into the following sections: in Section 1.1 we provide the definition of the LCR, in Section 1.2 we describe the scientific motivation for the LCR, and in Section 1.3 we outline the GRB classification. Then, in Section 2, we outline the data sample, the Willingale and BPL models (Section 2.1), and we report in detail the algorithms we used to obtain the reconstructed LCs, including the functional form toy model (Section 2.2) and the Gaussian processes (GPs; Section 2.3). The results are summarized in Section 3 for the functional form toy model approach (Section 3.1) and for the GPs (Section 3.2). We draw our conclusions in Section 4.

1.1. Light-curve Reconstruction

The LCR offers an innovative solution to the problem of temporal gaps in LCs. In several domains of astronomy, statistical LCR methods have been used to account for missing data. These LCR methods have also been applied to Cepheids using simulated annealing and Fourier decomposition techniques (Ngeow et al. 2003). A similar application of reconstruction methods on LCs can be seen in Huber et al. (2010) for planetary eclipse mapping and in Geiger & Schneider (1996) for the measurement of time delay in gravitational lens systems. However, an application of reconstruction techniques on GRB LCs has yet to be undertaken because GRB LCs have very variable features. They present a wide range of shapes, including smooth single pulses and multiple peaks with different widths occurring at different times, while others exhibit a more complex behavior.

As a first step of addressing this problem and evaluating the performance of LCR, we have used a relatively simple method that chooses a model to fit the LCs. Many groups have classified the LC morphology with a simple PL, BPL, smooth BPL, or W07 model; some with plateaus, and some with double breaks (Giblin et al. 2002; Nousek et al. 2006; De Pasquale et al. 2008; Evans et al. 2009; Liang et al. 2009; Racusin et al. 2009; Cenko et al. 2010). Although our results depend on the underlying model chosen for the reconstruction, we can give a first estimate of how the LCR can enhance the determination of the plateau parameters. Thus, we show how a more accurate morphological LC classification can be enabled and how the GRB parameters can be determined. Our LCR analysis reduced the uncertainties on the parameters of the plateau by 37.22% for a 10% noise level on average among all plateau parameters for the reconstruction with the W07 functional form toy model and by 30.69% for a 10% noise level for the BPL functional form toy model. Furthermore, using the GPs, the uncertainties on all plateau parameters are decreased by 31.43% for the W07 and 21.99% for the BPL, on average (see Section 3).

1.2. The Advantage of the Light-curve Reconstruction in Theoretical Models

We can anticipate that with the new reconstructed LCs, we can use them directly to test theoretical models. We here limit

ourselves to provide two examples because this topic is far beyond the current focus of the paper, and it will be investigated in a forthcoming paper. One of the most immediate advantages is the use of the parameters of the BPL obtained with the reconstructed LCs with GPs or the other functional toy model LCR modeling to test the standard fireball model via the closure relations, which are the relations among the temporal, α , and spectral indices, β , of the LCs. For a precise new estimate of the modeling, one could check the differences between the results obtained in X-rays from previous papers (Srinivasaragavan et al. 2020; Dainotti et al. 2021b) and those from the LCR. We envision that the prediction of the closure relations will be around 40% more accurate compared to the current estimate in the literature. Indeed, 43.32% is the percentage reduction of the uncertainty on the temporal index, α , after the plateau phase when we consider, for example, the W07 functional toy model for the reconstruction, and for the BPL, the uncertainty in the slope of the LC after the plateau phase, α_2 , decreases by 43.9%. For the GPs, the uncertainty in the W07 α parameter decreases by 41.5% and the uncertainty in the α_2 parameter decreases by 35.92%. There are cases for which it is not possible to uniquely determine the outcome of the closure relations, namely whether the closure relation favors a scenario with a fast or slow cooling, or if a constant medium or a wind medium is preferred. We can anticipate that a fraction of cases with the LCR will be able to discern the interstellar medium and the regime better and will be able to remove part of the degeneracy in the theoretical model investigation. Srinivasaragavan et al. (2020) found that >50% follow 11 out of the 16 closure relations tested. It is interesting to check how the exact percentage of fulfillment could change when LCR is adopted in this scenario. Another model that can benefit from the LCR is the magnetar model. Indeed, it was shown by Stratta et al. (2018) that due to the temporal gaps in some of the LCs, the magnetic field, the spin period parameters, or the electron energy fraction could not be determined very precisely; namely, their uncertainties are so large that the estimate cannot be considered reliable. In this scenario, it is important to have full coverage of the LC so that a combination of the magnetic field, the spin period, and the electron energy fraction could solve cases in which, due to these uncertainties on the parameters, it is even hard to distinguish between models (magnetars versus black hole). The LCR can alleviate the degeneracy of the parameters of the model by reducing the uncertainties of the parameters. However, some degree of degeneracy inherent to the model will still remain unavoidable. Here, we recall that this LCR will be approached as a first step, but it can also be extended in high-energy γ -rays, optical, and radio wavelengths for the determination of the closure relation in these respective energy bands (Dainotti et al. 2021d, 2022c, 2023a; Levine et al. 2023).

1.3. The Connection of the Light-curve Reconstruction and the Gamma-ray Burst Classification and Properties

The classification of GRB properties is often challenging because of the general lack of data points in the LC or, more often, for the lack of data points in a crucial part of the LC for which a feature is expected, e.g., the beginning or end of the plateau emission. This section aims to clarify how many GRBs classified in the literature as, for example, LGRBs, SGRBs, or the other classes defined below correspond to the

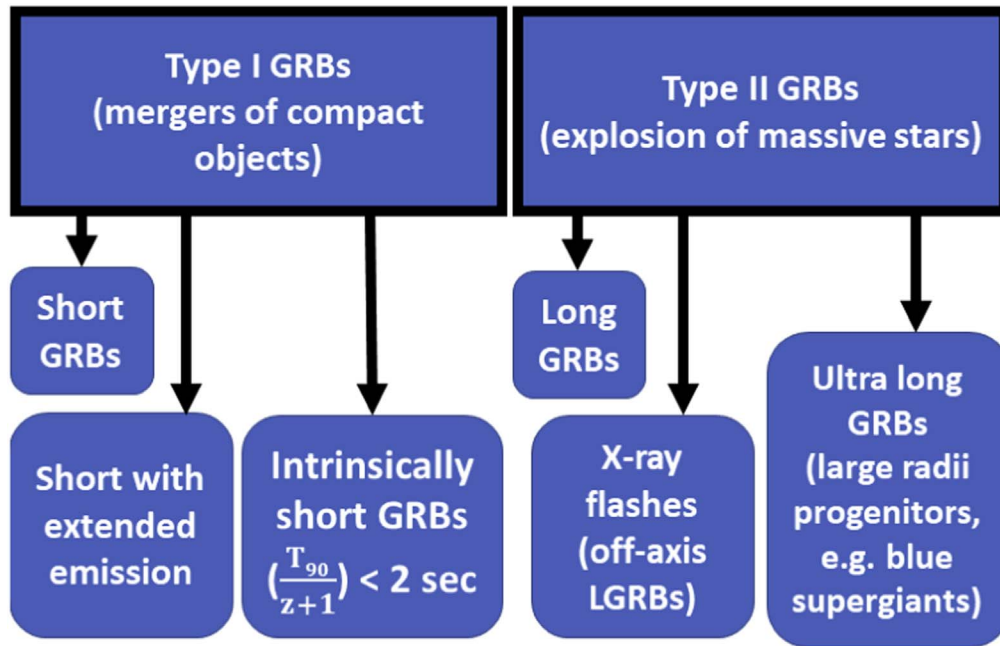


Figure 1. Schematic of GRB classes divided into Type I and Type II and their related subcategories.

morphological classes defined here. Indeed, this analysis is relevant because with this study, we can check the percentage of the good GRBs that fall in a given class.

In addition to the long and short classification, we point out that other subclasses have been discovered. Intrinsically SGRBs (IS) have $T_{90}/(1+z) < 2s$ (Levesque et al. 2010; Zhang et al. 2021; Rossi et al. 2022). SGRBs with extended emission (SEE; Norris et al. 2000; Norris & Bonnell 2006; Levan et al. 2007; Norris et al. 2010; Dichiaro et al. 2021) are SGRBs with mixed properties between LGRBs because they have $T_{90} > 2$ s, but they are harder in their spectral properties than the LGRBs, and in this regard, they are similar to SGRBs. From the observational point of view, they have a spike in the prompt followed by a long tail. The spike of the initial emission is followed by a brief pause in emission, lasting for $\simeq 10$ s, after which the emission increases again on a timescale of 30–50 s (Norris & Bonnell 2006). Ultralong GRBs (ULGRBs) have $T_{90} \geq 1000$ s (Gendre et al. 2013; Nakachi et al. 2013; Stratta et al. 2013; Levan et al. 2014; Piro et al. 2014; Zhang et al. 2014; Greiner et al. 2015; Kann et al. 2018; Gendre et al. 2019). These GRBs may originate from engine-driven explosions of stars much larger than LGRB progenitors (Levan et al. 2014). X-ray flashes (XRFs; Soderberg et al. 2004; Chincarini et al. 2010) are LGRBs with greater flux in X-rays (230 keV) than in γ -rays (30–400 keV), while X-ray rich (XRR) GRBs are an intermediate class between XRFs and LGRBs that display very strong X-ray emission. SNe-GRBs are LGRBs associated with SNe of type Ic (SNe Ic) for which the SNe has been clearly observed (Dainotti et al. 2007, 2022a). These subclasses may imply diverse progenitors or the same progenitor in different circumburst media.

Zhang et al. (2007a, 2007b, 2009) unified the classification in terms of progenitors, with Type I and Type II GRB classes. Type I includes SGRBs, SEE, and IS, and Type II includes LGRBs, XRFs, XRRs, GRB-SNe, and ULGRBs. For schematic pictures of the classes, see Figure 1.

Table 1
Full Sample of 455 GRBs, Including Redshift z , Observer-frame Burst Duration T_{90} , and Rest-frame Duration $\frac{T_{90}}{(1+z)}$ Long vs. Short Classification, GRB Type, and Reference

GRB NAME	z	T_{90}	$\frac{T_{90}}{(1+z)}$	Long/ Short	Type	Reference
GRB050128	...	28.00	...	L	SNe-GRB	(1)
GRB050315	1.95	95.40	32.35	L	XRR	(2)
GRB050318	1.44	40.00	16.37	L	XRR	(1)
GRB050319	3.24	151.74	35.79	L	XRF	(2)
GRB050401	2.90	33.30	8.54	L	L	(1)
GRB050416A	0.65	6.62	4.01	L	XRF/ SNe-GRB, D	(1), (3)
GRB050502B	5.20	17.72	2.86	L	XRR	(2)
GRB050505	4.27	58.90	11.18	L	L	(1)
GRB050607	...	48.00	...	L	XRR	(2)

References. (1) Sakamoto et al. (2008); (2) Bi et al. (2018); (3) Dainotti et al. (2022a) and additional references in the online table, including Dainotti et al. (2017); Dainotti et al. (2020a); Dainotti et al. (2021a); Gendre et al. (2019); Lien et al. (2016); Lipunov et al. (2018); Norris et al. (2010); Sakamoto et al. (2011); Tian et al. (2022); van Putten et al. (2014); Xu & Tang (2021); Yi et al. (2016), as well as GCN Circulars listed individually in the online table.

(This table is available in its entirety in machine-readable form.)

2. Method

We aim to fill temporal gaps in GRB LCs by compiling all observations from Swift XRT taken from the BAT+XRT repository. To account for the missing data points, we adopt a stochastic approach where the reconstructed points are built from a chosen LC model. To account for the realistic variation of the data, a noise function that considers the residuals from the initially observed flux data points is used to inject additive noise into the reconstructed points.

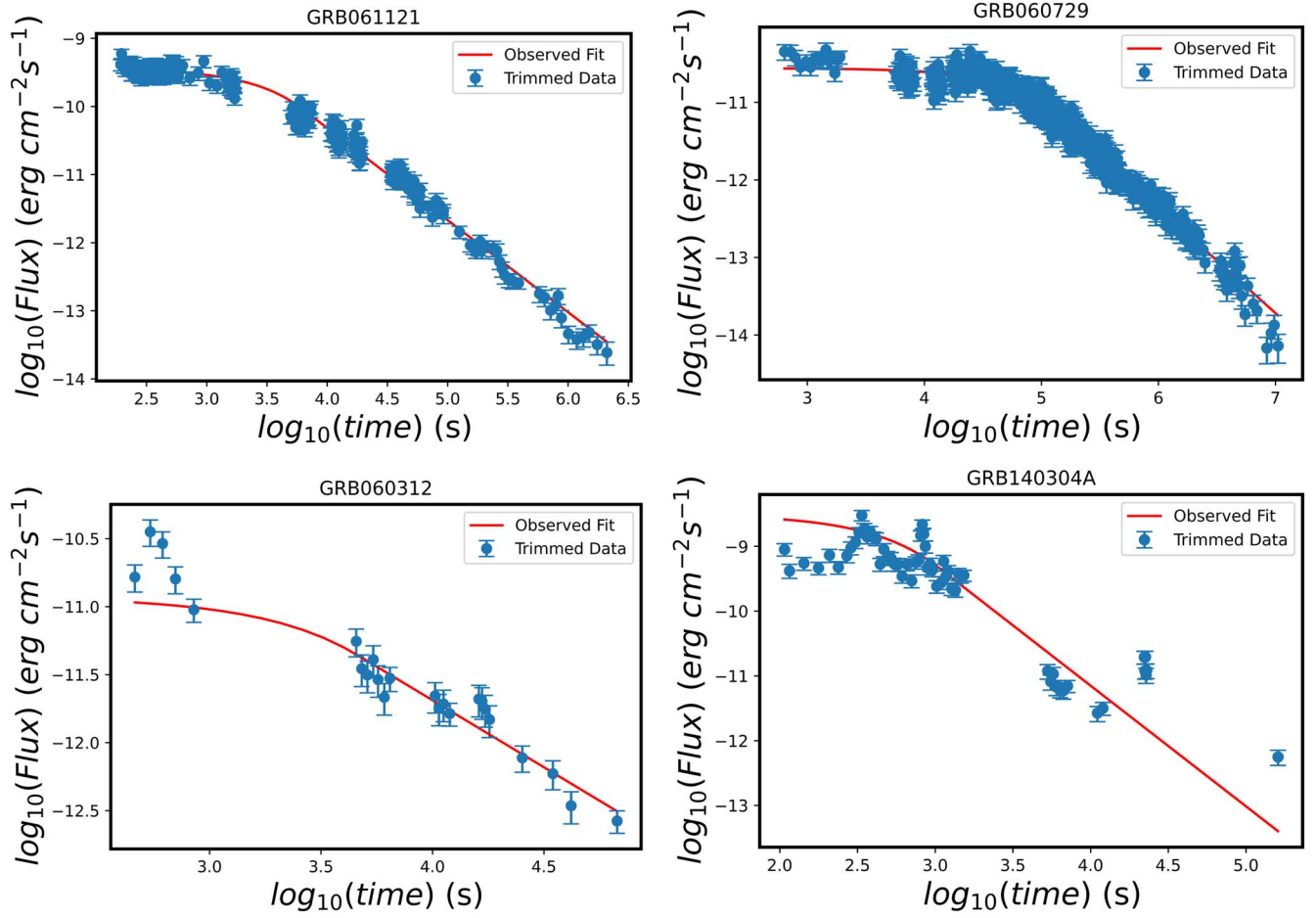


Figure 2. LCs divided into four categories depending on the afterglow feature. (i) good GRBs (top left); (ii) a break at the end of the LC (top right); (iii) flares/bumps in the afterglow (bottom left); and (iv) flares/bumps with a double break at the end of the LC (bottom right).

2.1. Data Sampling, the Willingale Model, and the Broken Power-law Model

We take a sample of 455 GRBs from Srinivasaragavan et al. (2020) with X-ray plateaus (222 with known redshift and 233 without known redshift), originally obtained from the Swift BAT-XRT repository (Evans et al. 2007, 2009). A sample of the data is presented in Table 1. These GRBs are fitted with the W07 function, described in Equation (1) as presented in Willingale et al. (2007),

$$f(t) = \begin{cases} F_i \exp\left(\alpha_i \left(1 - \frac{t}{T_i}\right)\right) \exp\left(-\frac{t}{t_i}\right) & \text{for } t < T_i \\ F_i \left(\frac{t}{T_i}\right)^{-\alpha_i} \exp\left(-\frac{t}{t_i}\right) & \text{for } t \geq T_i, \end{cases} \quad (1)$$

where T_i and F_i are the times and fluxes, respectively, either at the end of the prompt (denoted with p) or at the end of the plateau emission (denoted with a). The parameter α_i is the temporal index after T_i . The initial rise time is marked by the time t_i , which reads as t_a for the afterglow emission. The maximum flux occurs at $t_i = \sqrt{tT_c/a_i}$.

We also fit the GRBs with the simple BPL model,

$$f(t) = \begin{cases} F_i \left(\frac{t}{T_i}\right)^{-\alpha_1} & \text{for } t < T_i \\ F_i \left(\frac{t}{T_i}\right)^{-\alpha_2} & \text{for } t \geq T_i, \end{cases} \quad (2)$$

where T_i and F_i are the times and fluxes, respectively, at the break time (coincident with the end time of the plateau), α_1 is the slope of the LC before the break, and α_2 is the slope of the LC after the break. In both our Willingale and BPL fit, as in W07, we take the logarithm in base 10 of these functions.

We focus our reconstruction efforts on the plateau region of the GRB LCs, where our method works effectively. Before the plateau, the prompt emission has significant variability compared to the afterglow, and thus the prompt is difficult to model accurately. The stochastic approach used in this paper will also not account for flares and bumps in the afterglow because such variations are randomized to a very high degree. This is a first step toward understanding the feasibility of LCR. More complex methods that can generalize this first attempt to the prompt emission or flares in the afterglow phase will be explored in future works.

The 455 LCs were then separated into categories based on the afterglow features. For the subsequent analysis, we categorize the GRB afterglow LCs into those having (i) good approximation with the W07 model (hereafter called good GRBs), (ii) flares or bumps throughout the afterglow region, (iii) a double break at the end of the LC, and (iv) flares/bumps along with a double break. Figure 2 shows LCs belonging to each category with the W07 model fit superimposed. We take the Willingale function parameter values (for each GRB LC) from Srinivasaragavan et al. (2020).

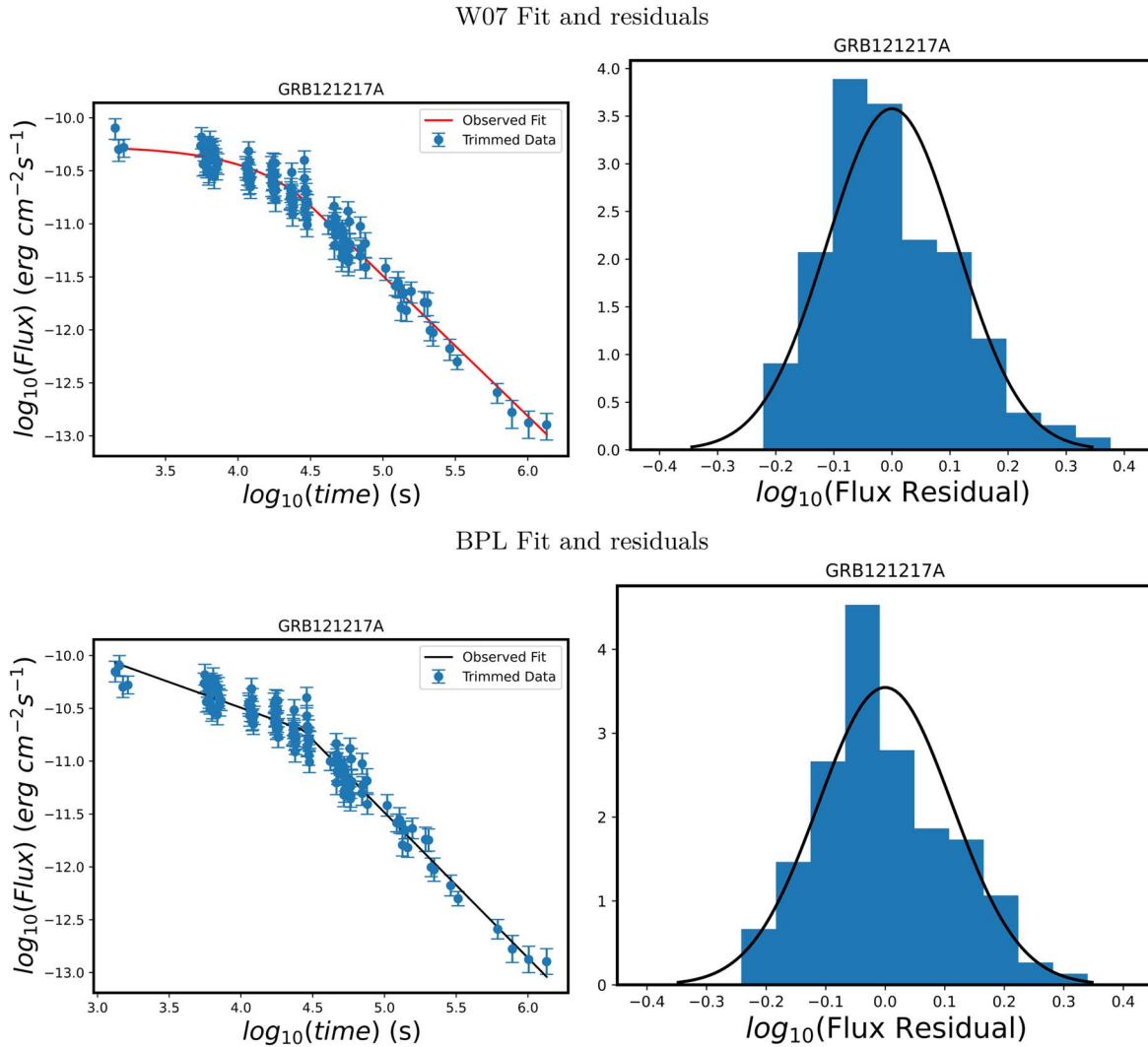


Figure 4. The left panels show the LCs of GRB GRB 121217A starting from the plateau emission, and the best-fit W07 model is shown in red in the upper panels and the BPL fit is shown in black in the lower panels. The right panels show the $\log(\text{flux})$ residual histogram, and the best-fit Gaussian distribution is shown in black.

We draw random variate samples from the fitted Gaussian to generate our reconstructed data points based on our previous assumption that the flux has Gaussian-distributed errors. We checked that the Gaussian is indeed the best-fit distribution with the Mathematica¹⁰ function `FindDistribution` and find that the values for normality for GRB121217A are $\mu = -0.0016$, and $\sigma = 0.12$.

For a given time, t , the reconstructed flux at that time is defined in Equation (5) as the sum of the fitted flux value and the noise based on the random variate sampled from the flux residual Gaussian distribution,

$$\log_{10} F_t^{\text{recon}} = \log_{10} f(t) + (1 + n) \times RV_N. \quad (5)$$

Here, F_t^{recon} is the reconstructed value of flux at time t , $f(t)$ is the W07 or BPL flux value at time t , n is the noise level, and RV_N is the random variate sampled from the normal (Gaussian) distribution.

We add the noise parameter to mimic the realistic variations seen in the observed LCs. We assume the noise to be stationary, meaning that the noise on the flux does not change with time and is random without temporal autocorrelation.

Usually, it is common to encounter cases in which the noise level is increased by 10% or 20%. We acknowledge that the choice of noise level is arbitrary, but the purpose here is to show how LCR works with realistic cases. Anyone with the detailed procedure we have described can change the noise level for the particular LCs they are reconstructing.

The RV_N for this noise is generated at every instant of time, starting from the beginning of the plateau from the distribution of the residuals fitted with a Gaussian. Thus, the reconstructed flux value is different for each point. In this manner, we can reconstruct data points within the temporal gaps of each LC.

Applying this method will result in all the reconstructed data points in the afterglow LC being, statistically, the same distance from the best fit of the W07 or BPL model as the initially observed data points. We choose the time of the reconstructed points along the fitting line with a time range distributed equally in the log scale. To this end, for practicality, we use the function in Python called `geomspace`, with the minimum and maximum time set at the beginning of the plateau and the last data point of the observed LC, respectively. Thus, each reconstructed LC is customized to each observed LC, which ensures the realistic nature of these reconstructed LCs for future use in cosmological studies.

¹⁰ Using Wolfram Mathematica 12.3.

Due to the random noise added to the reconstructed data points, we perform the reconstruction steps mentioned above for each GRB 100 times. This helps in derandomizing the results and stabilizing them. Then, the chosen function is fit on each iteration of the reconstructed LC, providing us with 100 new fit parameters and error estimates for each GRB. It should be noted that the new fit is performed on the LC, which contains the reconstructed flux and the original observations. So the combined LC is used here. The flux uncertainties for each reconstructed data point are generated randomly from a Gaussian distribution, which is the best-fit distribution of the uncertainties of the observed fluxes.

Thus, with the LCR procedure, we combine the reconstructed and original data points to create a new enhanced LC, which we refit with the chosen model with a least-squares regression. For this, we use the `minimize()` method from the `lmfit` library (Newville et al. 2016), which is an interface for fitting curves in Python. It is a further extension of the optimization techniques available in the methods of `scipy.optimize`. The `minimize()` function is used as an optimization function that minimizes the residuals to the fit line while doing the refitting. We provide this function with the model we wish to fit, the initial guess for the parameters, the data to fit (the reconstructed LCs), and the method to be used for the fitting. This function returns the updated values of the chosen model parameters and their associated uncertainties.

2.3. The Reconstruction Method with the Gaussian Processes

We briefly describe GPs and how we use them. GPs is a generic supervised-learning method that can generate precise predictions and is designed to solve regression problems. It is based on the mathematical properties of the Gaussian/normal distribution.

Due to its probabilistic nature, a GP model does not merely produce a singular prediction, but rather calculates the likelihood for each possible prediction.

A GP works on the postulates of Bayesian inference. It begins by inspecting the prior, which contains the leverage of knowledge of existing trends in the initial data, and using Bayesian inference to compute a posterior, a probabilistic description of the outcomes that agree with both the data and the prior. Each prediction has an associated confidence interval, which limits the region of the likelihood of the prediction.

The capacity to find confidence intervals/regions is the true utility of a GP model. The set of possible predictions might be a normal distribution with the mean as the model prediction and a variance that characterizes the deviation of the predictions from the mean. A lower uncertainty corresponds to a thinner confidence region, and the model is said to be confident with its prediction.

Covariance functions, also known as kernels, are a fundamental requirement for using a GP model. A kernel can be defined as a measure of the degree of similarity between two given input space data points. This contains the assumption that two similar data points should yield two similar output values. Kernels can be of different types: those depending directly on the difference between the two data points, that is, $x - x'$, and those depending on the specific values of the data points x and x' themselves. Kernels depending upon just their difference are translation-invariant in the input space. Furthermore, if the kernel in question merely depends on $|x - x'|$, then the kernel

is said to be isotropic in the input space. An example of such a kernel would be a radial basis function (RBF) kernel.

We here use the RBF plus the contribution of a white-noise kernel because we assume that the noises of the flux are independent and identically normally distributed. We use the built-in function *GaussianProcessRegressor*, which enables prediction without prior fitting, but only with prior knowledge of the GP. The prior in our analysis is not normalized, meaning that the mean is centered at zero. Here normalizing means that we would normalize the fluxes by removing the mean and scaling to unit-variance. We choose the default option as false. Then we fit the GP regression model with the built-in *fit* function to our data. Next, we have used the in-built *predict* function to obtain the reconstructed data points.

To reconstruct the LC with GP, we have chosen as the interval for the reconstruction the 95% confidence interval. We have populated the data points by using the Equation (5) again, but here the function $f(t)$, instead of being the W07 or the BPL function, is the function found via the GP. To avoid a strong dependence of the distribution of the data points in the GPs on the shape of the function obtained with the Gaussian regressor function, which is a built-in function in Python, we perform 100 Markov Chain Monte Carlo (MCMC) simulations of the reconstructed LC for each different LC. Then, we randomly pick one value for the data point and its associated uncertainty.

3. Results

3.1. Results from Functional Form Reconstruction

Applying our LCR method to the 218 good GRBs in our sample, we expect to see a reduction in the uncertainties on the chosen model parameters. To measure this, we compute the error fractions associated with each of the model parameters for the original and reconstructed fit. The error fractions for the three Willingale parameters are given by

$$EF_{\log_{10}(T_a)} = \left| \frac{\Delta \log_{10}(T_a)}{\log_{10}(T_a)} \right|, \quad (6)$$

$$EF_{\log_{10}(F_a)} = \left| \frac{\Delta \log_{10}(F_a)}{\log_{10}(F_a)} \right|, \quad (7)$$

$$EF_{\alpha_a} = \left| \frac{\Delta \alpha_a}{\alpha_a} \right|. \quad (8)$$

Here, EF_X is the error fraction associated with the parameter X , and ΔX is the uncertainty associated with the parameter X . The X and ΔX for $\log_{10}(T_a)$, $\log_{10}(F_a)$ and α_a before reconstruction are taken from Srinivasaragavan et al. (2020), as previously indicated.

The computed error fractions before and after reconstruction for the W07 model were performed for the full sample of 218 good GRBs for two noise levels, 10% and 20%, in Table 2. The first three columns show the error fraction for each W07 parameter from the original fitting. The second three columns show the error fraction for each W07 from the new fitting after reconstruction. These are averages of 100 iterations, as mentioned previously.

We calculate the percentage decrease in the error fractions for each noise level to analyze the improvement of the fit following the reconstruction. The formula used for the

Table 2

The Error Fractions of $\log_{10}(T_a)$, $\log_{10}(F_a)$ and α_a before and after Reconstruction (with Relative Percentage Decrease in Error for All Three Parameters) at 10% Noise ($n = 0.1$; Top) and 20% Noise ($n = 0.2$; Bottom)

GRB ID	$EF_{\log_{10}(T_a)}$	$EF_{\log_{10}(F_a)}$	EF_{α_a}	$EF_{\log_{10}(T_a)}$ RC	$EF_{\log_{10}(F_a)}$ RC	EF_{α_a} RC	$\%_{\log_{10}(T_a)}$	$\%_{\log_{10}(F_a)}$	$\%_{\alpha_a}$
10% noise									
050712	0.019	0.005	0.044	0.014	0.004	0.027	-26.67	-24.96	-38.04
050318	0.011	0.006	0.046	0.008	0.004	0.033	-22.91	-24.05	-28.62
050416A	0.024	0.005	0.018	0.016	0.003	0.012	-31.24	-33.54	-34.85
050607	0.021	0.005	0.044	0.016	0.004	0.027	-22.62	-22.79	-39.18
050713A	0.01	0.003	0.018	0.008	0.002	0.011	-16.21	-14.31	-36.35
050822	0.011	0.003	0.026	0.007	0.002	0.015	-31.06	-35.46	-43.07
050824	0.025	0.006	0.094	0.015	0.003	0.056	-40.7	-38.45	-40.27
050826	0.029	0.019	0.131	0.026	0.016	0.196	-9.54	-15.21	49.99
050915B	0.036	0.008	0.115	0.025	0.005	0.068	-29.03	-34.25	-40.92
051016A	0.033	0.006	0.051	0.021	0.004	0.024	-36.11	-28.49	-53
051109A	0.012	0.005	0.016	0.006	0.002	0.01	-51.32	-58.89	-33.99
051221A	0.02	0.005	0.051	0.015	0.004	0.033	-27.39	-28.33	-34.6
060105	0.004	0.001	0.007	0.003	0.001	0.003	-16.2	-14.1	-54.34
060108	0.024	0.006	0.071	0.018	0.004	0.047	-26.39	-30.58	-33.59
060109	0.014	0.005	0.057	0.008	0.003	0.025	-40.63	-45.09	-56.2
060124	0.008	0.004	0.012	0.006	0.003	0.007	-28.27	-29.34	-42.7
060218	0.028	0.014	0.082	0.014	0.005	0.065	-50.59	-63	-20.77
060306	0.012	0.003	0.024	0.009	0.002	0.017	-22.76	-28.7	-29.23
060418	0.018	0.005	0.03	0.01	0.003	0.01	-43.68	-32.48	-66.37
060421	0.041	0.01	0.087	0.022	0.006	0.039	-46.03	-40.58	-55.27
20% noise									
050712	0.019	0.005	0.044	0.014	0.004	0.028	-24.37	-22.28	-35.56
050318	0.011	0.006	0.046	0.009	0.004	0.034	-18.58	-19.74	-24.97
050416A	0.024	0.005	0.018	0.017	0.003	0.012	-27.39	-29.91	-31.97
050607	0.021	0.005	0.044	0.017	0.004	0.028	-17.04	-17.37	-36.04
050713A	0.01	0.003	0.018	0.009	0.003	0.012	-12.34	-10.16	-33.05
050822	0.011	0.003	0.026	0.008	0.002	0.015	-27.43	-32.13	-40.11
050824	0.025	0.006	0.094	0.016	0.004	0.059	-37.67	-35.27	-36.93
050826	0.029	0.019	0.131	0.025	0.014	0.172	-13.33	-28.04	31.46
050915B	0.036	0.008	0.115	0.027	0.006	0.073	-23.99	-30.54	-37.03
051016A	0.033	0.006	0.051	0.022	0.004	0.025	-32.78	-24.82	-50.61
051109A	0.012	0.005	0.016	0.006	0.002	0.011	-48.9	-56.82	-30.45
051221A	0.02	0.005	0.051	0.016	0.004	0.035	-23.51	-24.37	-31.17
060105	0.004	0.001	0.007	0.003	0.001	0.003	-11.94	-9.72	-51.99
060108	0.024	0.006	0.071	0.018	0.004	0.049	-23.82	-27.76	-30.82
060109	0.014	0.005	0.057	0.009	0.003	0.026	-37.84	-42.4	-54.15
060124	0.008	0.004	0.012	0.006	0.003	0.007	-23.7	-24.55	-40.13
060218	0.028	0.014	0.082	0.014	0.005	0.067	-48.31	-61.5	-18.12
060306	0.012	0.003	0.024	0.01	0.002	0.018	-20.13	-25.98	-26.29
060418	0.018	0.005	0.03	0.011	0.003	0.011	-41.52	-29.94	-64.95
060421	0.041	0.01	0.087	0.024	0.006	0.041	-41.96	-36.37	-52.87

Note. The first three columns give the error fraction for the original W07 fit, and the second three columns give the error fraction for new W07 fit after reconstruction. The final three columns give the percentage decrease in error fraction after reconstruction.

(This table is available in its entirety in machine-readable form.)

percentage decrease is given as

$$\%_{\text{DEC}} = \frac{|EF_X^{\text{after}}| - |EF_X^{\text{before}}|}{|EF_X^{\text{before}}|} \times 100. \quad (9)$$

The last three columns of Table 2 show the percent change in the error fraction after reconstruction for the two noise levels. From our analysis, we see that the error fraction on the reconstructed parameters is lower than the error fraction on the original parameters in all three cases. To better understand how this applies to the sample as a whole, we compute the average percentage decrease in error fraction for all good GRBs tested at each noise level. For the 10% noise level, we obtain a

33.33% decrease in the error fraction on the $\log(T_a)$ parameter, a 35.03% decrease in the error fraction on the $\log(F_a)$ parameter, and a 43.32% decrease in the error fraction on the α parameter. For the 20% noise level, we obtain a 29.49% decrease in the error fraction on the $\log(T_a)$ parameter, a 31.24% decrease in the error fraction on the $\log(F_a)$ parameter, and a 40.57% decrease in the error fraction on the α parameter. As expected, when we introduce a higher noise level, the decrease on the uncertainty also decreases because the spread around the best-fit line increases.

A visual comparison between two noise levels for a sample GRB, GRB121217A, for 10% and 20% of the W07 fit is shown in the upper panels of Figure 5. We observe that lower

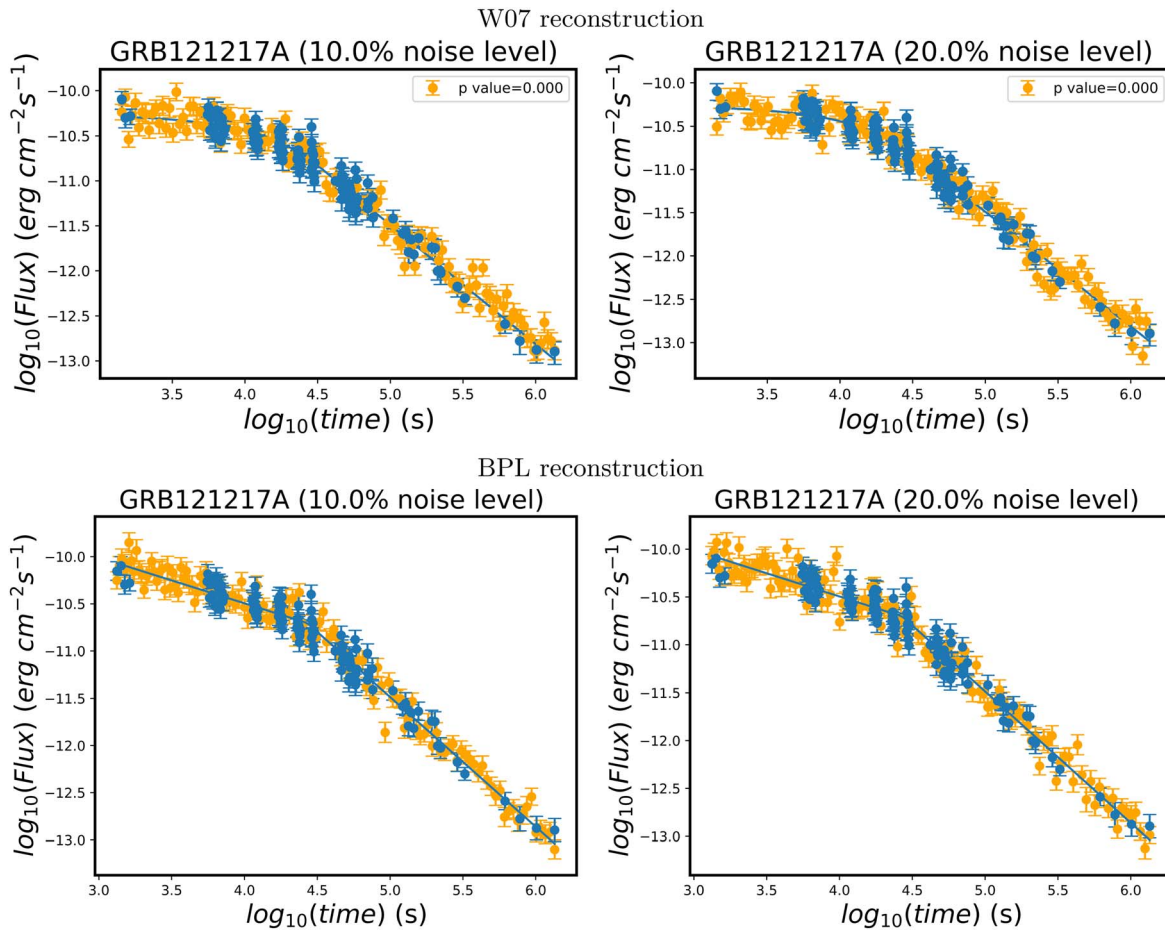


Figure 5. Reconstructed LCs for GRB121217A at two noise levels, using the W07 and BPL fits. The first row shows the reconstructed LCs using the W07 model at 10% and 20% noise, and the bottom row show the reconstructed LCs using the BPL model at 10% and 20% noise. These data points are generated from the noise distribution produced by fitting a Gaussian distribution on the flux residual histograms.

noise levels generate points somewhat close to the W07 fit, and these points are further spread out as the noise level increases. The reconstructed LC plots are picked randomly from the 100 reconstructions for each GRB. As expected, we can approximate the flux uncertainties with a Gaussian distribution, as shown in Figure 6. The histograms of Figure 7 show the distribution of the percentage decrease (the upper panel shows the 10% noise level, and the bottom panel shows the 20% noise level) for all three of the W07 parameters. As is evident, the reconstruction leads to a decrease in the errors on the W07 parameters for all the GRBs. After fitting the model, we expect a decrease in the uncertainty because we are refitting more points with the same model. However, the point of this approach is to provide a first simple solution to the LCR. This toy model for the reconstruction is indeed model dependent, but in principle, this method can work on any model.

To assess the dependence of the method on a particular model, we also fit with the BPL model and check the differences regarding the decrease in the uncertainties. To test the BPL, we perform the same method as used on the W07 fits. Again, we see an overall decrease in the error fraction on the reconstructed parameters as compared to the error fraction on the original parameters. We again compute the average percentage decrease in the error fraction for all good GRBs tested at each noise level. For the 10% noise

level, we obtain a 33.31% decrease in the error fraction on the $\log(T_a)$ parameter, a 30.79% decrease in the error fraction on the $\log(F_a)$ parameter, a 14.76% decrease in the error fraction on the α_1 parameter, and a 43.98% decrease in the error fraction on the α_2 parameter. For the 20% noise level, we obtain a 29.88% decrease in the error fraction on the $\log(T_a)$ parameter, a 27.20% decrease in error fraction on the $\log(F_a)$ parameter, a 1.78% decrease in the error fraction on the α_1 parameter, and a 41.1% decrease in the error fraction on the α_2 parameter.

Overall, we see a similar trend to the W07 fitting. The results for the average change in error fraction for the BPL fitting are given in Table 3. The comparison between two noise levels for a sample GRB, GRB121217A, for 10% and 20% of the BPL fit is shown in the lower panels of Figure 5. Figure 8 shows the distribution of the percentage decrease (the upper panel shows the 10% noise level, and the bottom panel shows the 20% noise level) for all four of the BPL parameters. Again, the reconstruction leads to a decrease in the uncertainties on the BPL parameters for all the GRBs. The average percentage decrease on all parameters for both the W07 and BPL fits is summarized in Table 4.

We also check the differences between the GPs (a completely model-independent approach) and the BPL (a model-dependent approach) to assess the differences between these methods.

GRB121217A

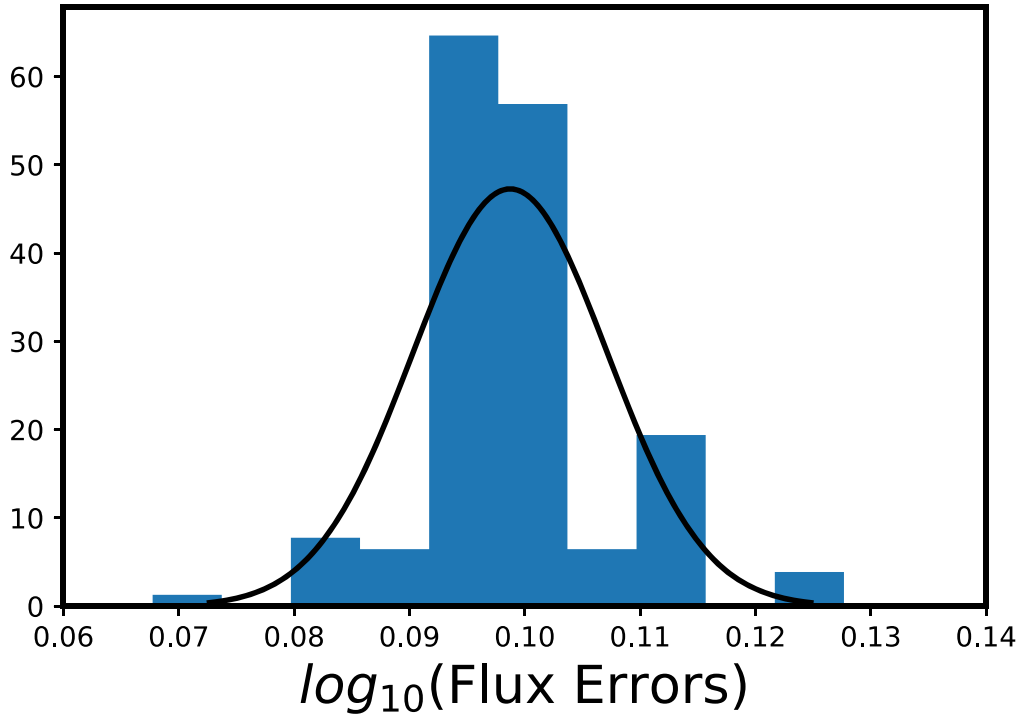
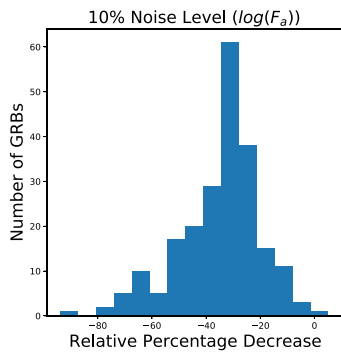
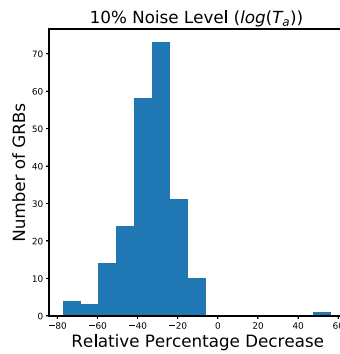


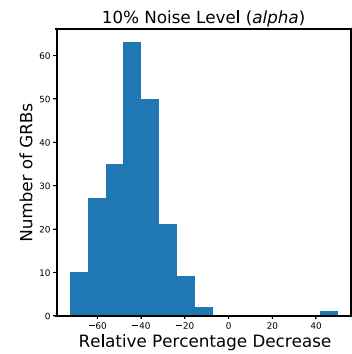
Figure 6. Histogram of the error bars of the observed fluxes, shown to be approximated with a Gaussian distribution.



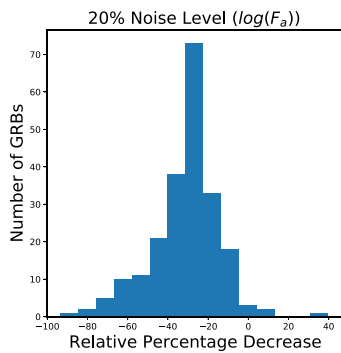
(a) Distribution of the 10% noise level for the $\log F_a$ with W07.



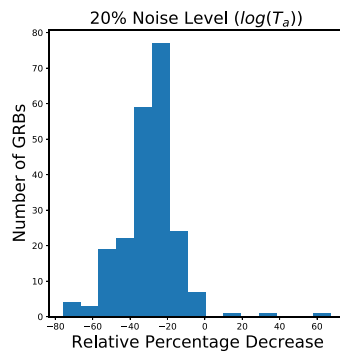
(b) Distribution of the 10% noise level for the $\log T_a$ with W07



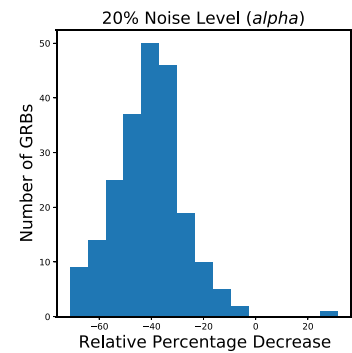
(c) Distribution of the 10% noise level for the α_a with W07



(d) Distribution of the 20% noise level for the $\log F_a$ with the W07



(e) Distribution of the 20% noise level for the $\log T_a$ with W07



(f) Distribution of the 20% noise level for the α with W07

Figure 7. Distribution of the relative percentage decrease for the parameters of the W07 function when we apply the W07 for the reconstruction.

Table 3

The Error Fractions of $\log_{10}(T_a)$, $\log_{10}(F_a)$, α_1 and α_2 before and after Reconstruction (with the Relative Percentage Decrease in the Error for All Three Parameters) at 10% Noise ($n = 0.1$; Top) and 20% Noise ($n = 0.2$; Bottom)

GRB ID	$EF_{\log_{10}(T)}$	$EF_{\log_{10}(F)}$	EF_{α_1}	EF_{α_2}	$EF_{\log_{10}(T)}$ RC	$EF_{\log_{10}(F)}$ RC	EF_{α_1} RC	EF_{α_2} RC	$\%_{\log_{10}(T)}$	$\%_{\log_{10}(F)}$	$\%_{\alpha_1}$	$\%_{\alpha_2}$
10% noise												
GRB050712	0.031	0.031	0.155	0.056	0.022	0.008	0.158	0.033	-30.6	-28.48	2.15	-39.97
GRB050318	0.011	-0.007	0.075	0.047	0.009	0.005	0.058	0.038	-20.09	-23.11	-23.14	-19.47
GRB050416A	0.038	-0.01	0.078	0.023	0.029	0.007	0.056	0.013	-23.52	-22.5	-28.03	-40.54
GRB050607	0.036	-0.011	0.15	0.053	0.03	0.01	0.166	0.03	-16.39	-11.78	10.48	-43.15
GRB050713A	0.015	-0.006	0.043	0.019	0.012	0.004	0.039	0.013	-18.58	-18.89	-9.77	-34.12
GRB050822	0.012	-0.004	0.223	0.024	0.01	0.004	0.164	0.014	-14.58	-14.2	-26.57	-42.26
GRB050824	0.026	-0.006	0.276	0.105	0.015	0.004	0.223	0.057	-40.25	-30.63	-19.2	-46.1
GRB050826	0.008	-0.004	0.328	0.064	0.005	0.002	0.226	0.039	-33.14	-35.02	-30.9	-38.46
GRB050915B	0.021	-0.006	0.085	0.13	0.012	0.004	0.057	0.069	-43.28	-33.53	-32.4	-46.8
GRB051016A	0.089	-0.025	0.327	0.048	0.047	0.013	0.2	0.024	-47.27	-48.27	-38.99	-49.86
GRB051109A	0.011	-0.005	0.136	0.015	0.009	0.003	0.049	0.01	-21.7	-24.17	-63.81	-31.43
GRB051221A	0.021	-0.007	0.082	0.058	0.016	0.006	0.067	0.038	-23.99	-23.82	-18.86	-34.93
GRB060105	0.007	-0.002	0.011	0.011	0.003	0.002	0.011	0.003	-51.9	-34.29	8.85	-68.73
GRB060108	0.026	-0.008	0.147	0.075	0.019	0.006	0.113	0.048	-26.83	-25.54	-23.34	-36.11
GRB060109	0.01	-0.003	0.347	0.047	0.007	0.003	0.271	0.022	-26.18	-9.85	-22.03	-54.26
GRB060124	0.014	-0.008	0.034	0.019	0.011	0.007	0.027	0.01	-17.7	-16.08	-21.58	-47.95
GRB060218	0.013	-0.005	0.582	0.064	0.01	0.004	0.811	0.042	-22.2	-21.99	39.27	-34.22
GRB060306	0.075	-0.026	0.395	0.024	0.018	0.006	0.107	0.018	-76.3	-78.27	-72.97	-24.73
GRB060418	0.066	-0.034	0.11	0.029	0.029	0.014	0.054	0.011	-56.32	-57.75	-51.17	-64.14
GRB060421	0.092	-0.038	0.557	0.082	0.04	0.015	0.249	0.041	-56.87	-59.92	-55.33	-50.46
20% noise												
GRB050712	0.031	-0.011	0.155	0.056	0.022	0.008	0.161	0.035	-28.73	-25.69	3.85	-37.46
GRB050318	0.011	-0.007	0.075	0.047	0.009	0.006	0.061	0.039	-16.43	-19.69	-19.51	-17.34
GRB050416A	0.038	-0.01	0.078	0.023	0.03	0.008	0.06	0.014	-20.36	-19.71	-23.32	-38.02
GRB050607	0.036	-0.011	0.15	0.053	0.031	0.01	0.175	0.032	-13.92	-9.42	16.3	-40.4
GRB050713A	0.015	-0.006	0.043	0.019	0.012	0.005	0.04	0.013	-15.14	-15.83	-7.65	-30.87
GRB050822	0.012	-0.004	0.223	0.024	0.011	0.004	0.176	0.015	-10.2	-9.64	-21.26	-39.39
GRB050824	0.026	-0.006	0.276	0.105	0.016	0.005	0.243	0.06	-36.94	-26.72	-11.73	-43.25
GRB050826	0.008	-0.004	0.328	0.064	0.005	0.003	0.228	0.041	-29.66	-32.24	-30.38	-35.41
GRB050915B	0.021	-0.006	0.085	0.13	0.012	0.004	0.059	0.071	-42.53	-31.23	-30.44	-45.47
GRB051016A	0.089	-0.025	0.327	0.048	0.049	0.013	0.199	0.025	-44.35	-45.47	-39.16	-48.04
GRB051109A	0.011	-0.005	0.136	0.015	0.009	0.004	0.051	0.011	-18.25	-20.91	-62.47	-28.61
GRB051221A	0.021	-0.007	0.082	0.058	0.017	0.006	0.071	0.04	-19.03	-18.86	-14.41	-31.45
GRB060105	0.007	-0.002	0.011	0.011	0.004	0.002	0.012	0.004	-49.46	-30.98	14.36	-67.13
GRB060108	0.026	-0.008	0.147	0.075	0.02	0.006	0.12	0.05	-24.59	-22.87	-18.53	-33.57
GRB060109	0.01	-0.003	0.347	0.047	0.008	0.003	0.291	0.023	-22.04	-4.53	-16.26	-51.69
GRB060124	0.014	-0.008	0.034	0.019	0.012	0.007	0.029	0.01	-13.29	-11.75	-15.88	-45.85
GRB060218	0.013	-0.005	0.582	0.064	0.01	0.004	0.876	0.045	-17.72	-17.19	50.51	-30.2
GRB060306	0.075	-0.026	0.395	0.024	0.018	0.006	0.108	0.019	-75.59	-77.65	-72.61	-20.71
GRB060418	0.066	-0.034	0.11	0.029	0.03	0.015	0.056	0.011	-53.89	-55.46	-49.07	-62.74
GRB060421	0.092	-0.038	0.557	0.082	0.041	0.016	0.262	0.041	-55.29	-58.42	-53.06	-50.02

Note. The first three columns give the error fraction for the original BPL fit, and the second three columns give the error fraction for the new W07 fit after reconstruction. The final three columns give the percentage decrease in the error fraction after reconstruction.

(This table is available in its entirety in machine-readable form.)

3.2. Results from Gaussian Process Reconstruction

The GP-based reconstruction provides a model-independent way of achieving our aim. The reconstructed LC of GRB121217A is presented in Figure 9. Following the reconstruction, the full LC is fitted with both the W07 and the BPL model to obtain new estimates of the parameters and their errors.

For the parameter $\log(T_a)$, we observe an average decrease in the error fraction of 25%. Similarly, for $\log(F_a)$ and α , the average decreases in the error fraction are 27.9% and 41.5%,

respectively. Note that in this case, the error fractions are also calculated according to Equation (9). The histogram distributions of Figure 10 show the distribution of the relative percentage decrease of the three W07 parameters. The results of the GP for the W07 are given for each GRB in Table 5, and the average percentage decrease on the uncertainties of the parameters for all GRBs are presented in Table 4.

For the BPL fits, we see that for the α_1 parameter, there is occasionally an increase in the error fraction from the original parameters to the reconstructed parameters. This is because the

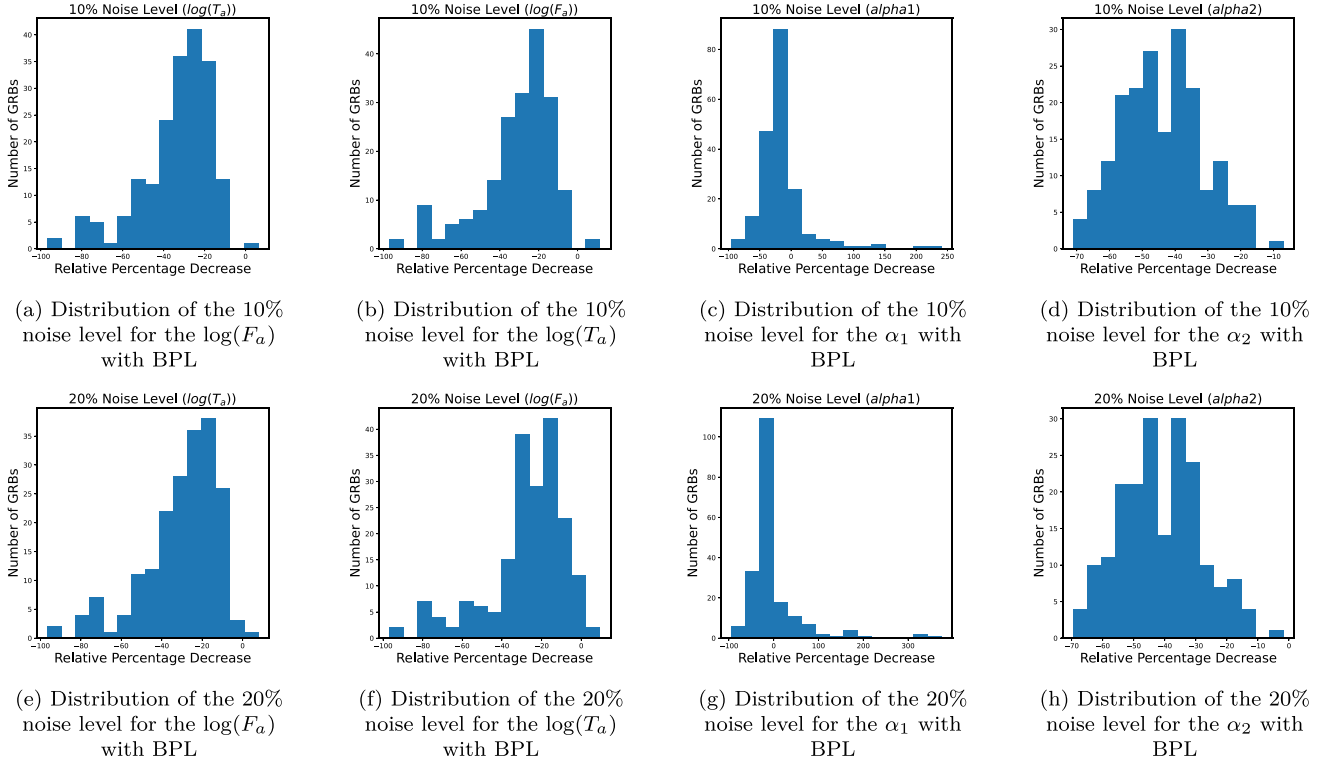


Figure 8. Distribution of the relative percentage decrease for the parameters of the BPL fit when we apply the BPL for the reconstruction.

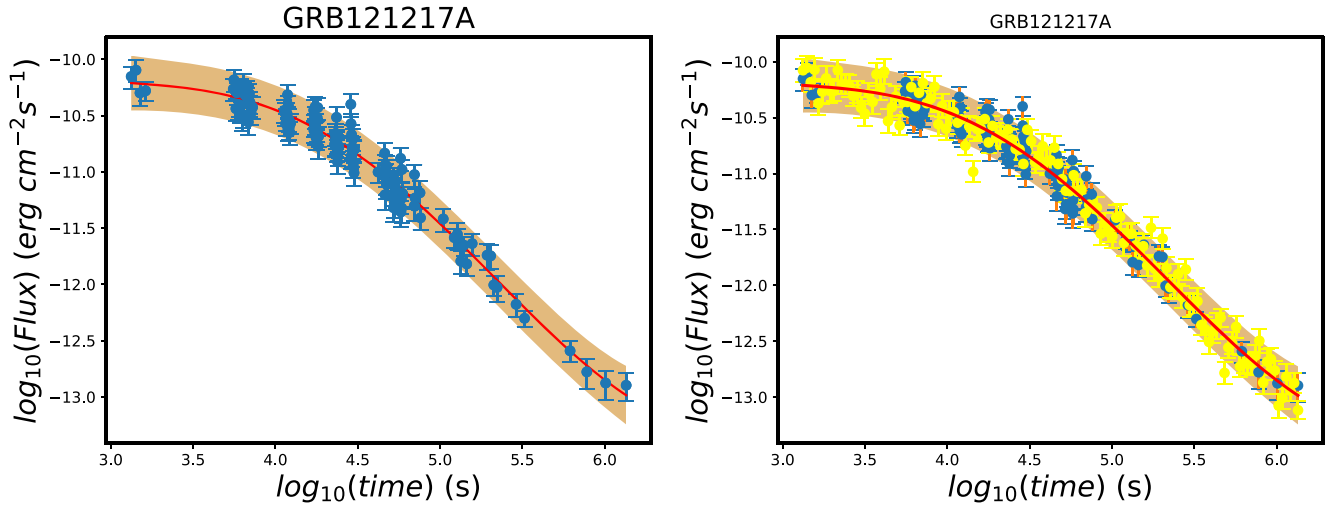


Figure 9. Gaussian process for the GRB 121217A. The left panel shows the GP fit, and the right panel shows the reconstructed LCs.

Table 4
The Average Percentage Decrease in the Error Fractions for the Various Parameters, Following the Reconstruction

Reconstruction Process	$\%_{\log_{10}(T_a)}^{\text{avg}}$	$\%_{\log_{10}(F_a)}^{\text{avg}}$	$\%_{\alpha_1}^{\text{avg}}$	$\%_{\alpha_2}^{\text{avg}}$
W07 reconstruction (10%)	-33.33	-35.03	-43.32	...
W07 reconstruction (20%)	-29.49	-31.24	-40.57	...
BPL reconstruction (10%)	-33.3	-30.78	...	-14.76
BPL reconstruction (20%)	-29.88	-27.2	...	-1.7
Gaussian process (W07)	-24.9	-27.9	-41.5	...
Gaussian process (BPL)	-15.02	-11.91	...	-25.10

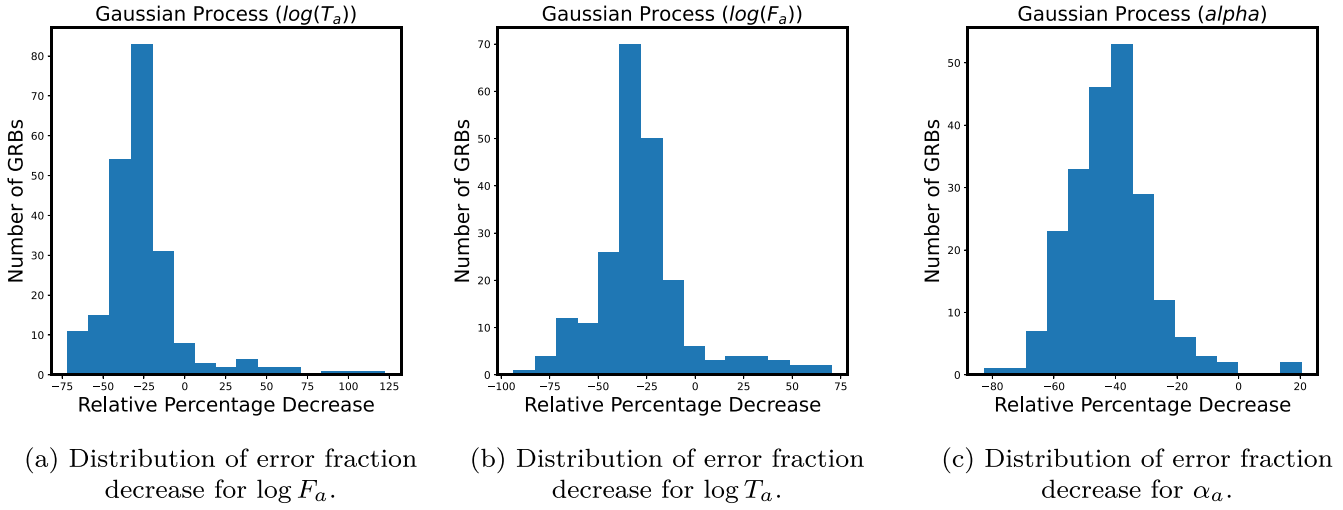


Figure 10. Distribution of the relative percentage decrease for the parameters of the W07 function following GP reconstruction.

Table 5

The W07 Error Fractions of $\log_{10}(T_a)$, $\log_{10}(F_a)$ and α_a before and after Performing the GP Reconstruction (with the Relative Percentage Decrease in Error for All Three Parameters)

GRB ID	$EF_{\log_{10}(T_i)}$	$EF_{\log_{10}(F_i)}$	EF_{α_i}	$EF_{\log_{10}(T_i)}$ RC	$EF_{\log_{10}(F_i)}$ RC	EF_{α_i} RC	$\%_{\log_{10}(T_i)}$	$\%_{\log_{10}(F_i)}$	$\%_{\alpha_i}$
GP (W07)									
050712	0.019	0.005	0.044	0.012	0.003	0.028	-34.01	-31.09	-36.97
050318	0.011	0.006	0.046	0.008	0.004	0.031	-26.66	-27.68	-32.19
050416A	0.024	0.005	0.018	0.016	0.003	0.011	-32.44	-34.04	-38.46
050607	0.021	0.005	0.044	0.017	0.004	0.028	-18.58	-19.62	-36.98
050713A	0.01	0.003	0.018	0.008	0.002	0.011	-18.81	-15.29	-35.28
050822	0.011	0.003	0.026	0.008	0.002	0.015	-29.98	-33.14	-43.56
050824	0.025	0.006	0.094	0.015	0.003	0.056	-39.2	-37.19	-40.83
050826	0.029	0.019	0.131	0.02	0.012	0.156	-32.22	-36.64	19.63
050915B	0.036	0.008	0.115	0.024	0.005	0.068	-34.36	-37.46	-41.29
051016A	0.033	0.006	0.051	0.024	0.005	0.025	-25.01	-17.02	-51.08
051109A	0.012	0.005	0.016	0.007	0.002	0.009	-41.5	-49.53	-40.98
051221A	0.02	0.005	0.051	0.013	0.004	0.033	-33.79	-32.68	-34.76
060105	0.004	0.001	0.007	0.003	0.001	0.003	-23.04	-20.31	-52.2
060108	0.024	0.006	0.071	0.018	0.004	0.047	-23.29	-28.84	-33.57
060109	0.014	0.005	0.057	0.008	0.003	0.025	-40.9	-44.23	-55.74
060124	0.008	0.004	0.012	0.005	0.003	0.007	-34.32	-34.36	-45.13
060218	0.028	0.014	0.082	0.013	0.005	0.062	-54.56	-65.62	-24.38
060306	0.012	0.003	0.024	0.01	0.002	0.018	-19.95	-26.66	-26.92
060418	0.018	0.005	0.03	0.009	0.003	0.01	-48.49	-37.4	-67.46
060421	0.041	0.01	0.087	0.032	0.008	0.046	-21.65	-20.75	-46.81

Note. The first three columns give the error fraction for the original W07 fit, and the second three columns give the error fraction for the new W07 fit after GP reconstruction. The final three columns give the percentage decrease in the error fraction after GP reconstruction.

(This table is available in its entirety in machine-readable form.)

slope of the LC before the break in the BPL fitting can be very flat, which will cause the uncertainty to be high compared to the α_1 value and cause the error fraction to be >1 . Because of this, we remove the GRBs that exhibit a flat α_1 or $|\alpha_1| < 0.1$. We see a percentage decrease in the parameters of 15.02% for $\log(T_a)$, 11.91% for $\log(F_a)$, 25.10% for α_1 , and 35.92% for α_2 . Again, the BPL fitting results show a similar trend to the W07 fits. The histogram distributions of Figure 11 show the distribution of the relative percentage decrease of the four BPL parameters. The results of the GP for each GRB are given in Table 6, and the average percentage decrease in the uncertainties of the parameters for all GRBs are given in Table 4.

4. Summary and Conclusion

We propose a relatively simple method for GRB LCR for LCs with X-ray plateaus observed by Swift. This case study involves two functional form toy models, the W07 and the BPL model and a limited GRB sample, as the main aim is to open the way for a new method that can be tested with more fitting functions and different statistics (e.g., Bayesian) in the future.

Our method assumes the W07 and the BPL models as the starting model for reconstruction, but the method presented here is versatile and can be extended to any other model (smooth BPL, double BPL, etc). Even models such as the pulse model, which includes the prompt emission, can be explored in the future. We also took a further step in the analysis adopting GPs

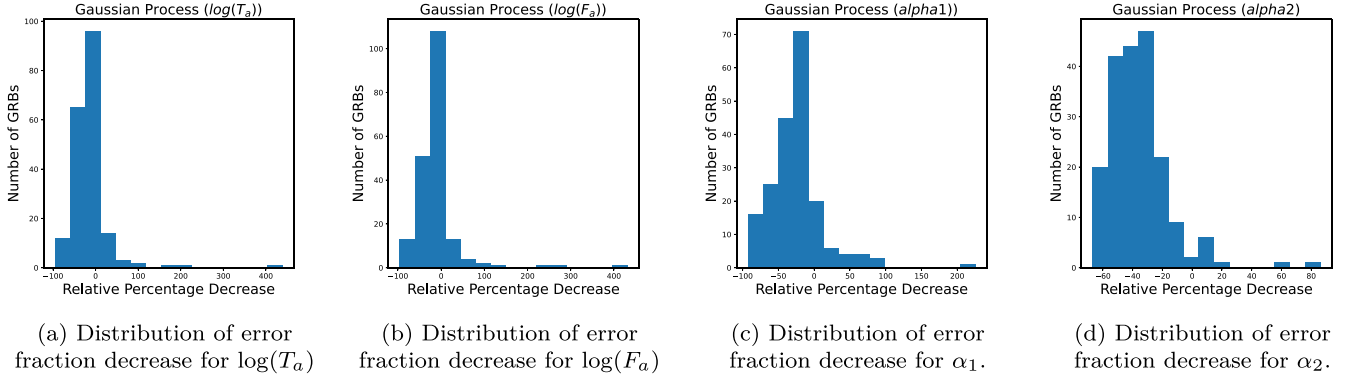


Figure 11. Distribution of the relative percentage decrease for the parameters of the BPL function following GP reconstruction.

Table 6
Data for the BPL Fit of the GP-based Reconstruction

GP (BPL)													
GRB ID	$EF_{\log_{10}(T_i)}$	$EF_{\log_{10}(F_i)}$	EF_{α_1}	EF_{α_2}	$EF_{\log_{10}(T_i)}$ RC	$EF_{\log_{10}(F_i)}$ RC	EF_{α_1} RC	EF_{α_2} RC	$\%_{\log_{10}(T_i)}$	$\%_{\log_{10}(F_i)}$	$\%_{\alpha_1}$	$\%_{\alpha_2}$	
050712	0.031	-0.011	0.155	0.056	0.02	0.008	0.114	0.035	-36.96	-31.16	-26.56	-36.7	
050318	0.011	-0.007	0.075	0.047	0.009	0.005	0.057	0.037	-21.44	-24.84	-25.07	-22.08	
050416A	0.038	-0.01	0.078	0.023	0.03	0.008	0.054	0.013	-22.17	-20.55	-30.49	-41.1	
050607	0.036	-0.011	0.15	0.053	0.033	0.01	0.265	0.03	-9.03	-6.18	76.48	-44.07	
050713A	0.015	-0.006	0.043	0.019	0.012	0.005	0.038	0.013	-19.09	-17.92	-10.82	-33.81	
050822	0.012	-0.004	0.223	0.024	0.011	0.004	0.126	0.014	-13.12	-10.96	-43.37	-40.74	
050824	0.026	-0.006	0.276	0.105	0.016	0.004	0.257	0.056	-36.37	-29.54	-6.94	-47.22	
050826	0.008	-0.004	0.328	0.064	0.009	0.004	0.387	0.068	18.19	10	18.16	6.79	
050915B	0.021	-0.006	0.085	0.13	0.017	0.005	0.068	0.085	-19.3	-12.5	-19.55	-34.08	
051016A	0.089	-0.025	0.327	0.048	0.055	0.016	0.123	0.029	-38.03	-36.85	-62.33	-38.73	
051109A	0.011	-0.005	0.136	0.015	0.009	0.004	0.043	0.01	-17.46	-18.84	-67.92	-33.14	
051221A	0.021	-0.007	0.082	0.058	0.015	0.005	0.062	0.038	-29.47	-27.45	-24.21	-34.37	
060105	0.007	-0.002	0.011	0.011	0.004	0.002	0.012	0.004	-47.21	-29.55	16.34	-66.73	
060108	0.026	-0.008	0.147	0.075	0.02	0.006	0.13	0.05	-21.43	-19.39	-11.85	-33.82	
060109	0.01	-0.003	0.347	0.047	0.008	0.003	0.249	0.022	-22.93	-1	-28.48	-52.56	
060124	0.014	-0.008	0.034	0.019	0.012	0.007	0.026	0.009	-15.57	-14.13	-24.78	-49.47	
060218	0.013	-0.005	0.582	0.064	0.011	0.004	0.551	0.045	-16.69	-15.08	-5.28	-29.79	
060306	0.075	-0.026	0.395	0.024	0.017	0.005	0.092	0.019	-77.62	-79.69	-76.75	-20.34	
060418	0.066	-0.034	0.11	0.029	0.031	0.015	0.068	0.01	-52.96	-55.91	-38.76	-64.8	
060421	0.092	-0.038	0.557	0.082	0.053	0.02	0.177	0.051	-43.01	-46.22	-68.23	-37.96	

Note. The BPL error fractions of $\log_{10}(T_a)$, $\log_{10}(F_a)$, α_1 , and α_2 before and after GP reconstruction (with the relative percentage decrease in the error for all three parameters). The first four columns give the error fraction for the original BPL fit, and the second four columns give the error fraction for the new BPL fit after GP reconstruction. The final four columns give the percentage decrease in the error fraction after reconstruction.

(This table is available in its entirety in machine-readable form.)

with the aim of being completely model independent. We find that after testing our method on a sample of 218 good GRBs, we obtain a reduction in the error bars of the plateau parameters of the W07 fitting—in this case, we have a reduction of 37.22% on average for all parameters when the noise is set at the 10% level, and a 33.77% reduction, on average, for all parameters with a 20% noise level. Regarding the BPL, we have a reduction of 30.69% on average for the 10% noise level and a reduction of 24.97% for the 20% noise level. For the GP, we have a decrease of 31.43% for the W07 and 21.99% for the BPL on average. The reduction of the uncertainties on the plateau parameters can be crucial for many cosmological studies that benefit from precise measurements of these parameters, including the investigation of Population III stars or the use of GRBs as standard candles to study the early Universe.

There are many advantages for the community from our study because filling in the temporal gaps of observed LCs with

a toy model solves the problem of the lack of data and thus allows us to use the reconstructed LC for

1. discovering plateau features in GRB LCs, which otherwise may remain undetected,
2. increasing the sample size for building GRB correlations among the plateau parameters,
3. testing theoretical models that would use the reconstructed LCs because the method is general and can be used with many different functions,
4. cosmological studies to reduce the scatter on the cosmological parameters. This will be achieved using the enhanced GRB correlations involving the plateau emission built with LCR,
5. estimating the redshift information with a machine-learning analysis that uses the new, more accurate estimates of the plateau parameters. This can allow us

to determine the redshift of the high- z GRBs and thus further enhance the studies of Population III stars,



6. and a classification of GRBs according to their morphology with increased accuracy.

As a final remark, this reconstruction is based on the LCs provided by Swift, but it can be extended to any current or future missions and across different wavelengths as well.

Acknowledgments

This work was made possible in part by the United States Department of Energy, Office of Science, Office of Workforce Development for Teachers and Scientists (WDTS) under the Science Undergraduate Laboratory Internships (SULI) program, which funded the initial help in creating the code for the reconstructed LCs of Luke Nearhood and Sarvesh Gharat. We thank Malgorzata Bogdan for helpful comments and discussion of our analysis. We also thank Susrestha Paul, Anish Kalsi, Shubham Bhardwaj, and Sachin Venkatesh for their help in the GRB classification. We are particularly grateful to Artem Poliszczuk for the initial discussion on the manuscript. We would also like to thank Dr. J. Xavier Prochaska for his helpful discussion of the Gaussian processes. This research was also supported by the Visibility and Mobility module of the Jagiellonian University (grant No. WSPR.WSDNSP.2.5.2022.5) and the NAWA STER Mobility grant (No. PPI/STE/2020/1/00029/U/00001). A.N. and M.G.D are grateful for the Exploratory Research Grant (ERF) of the Division of Science at NAOJ for the financial support of the visit of A.N. A.N. is also extremely grateful to NAOJ for providing all the essential amenities during the visit to the NAOJ Mitaka Campus. D.L. is also grateful for the support of the ERF grant. This work was also supported by the Polish National Science Centre grant UMO-2018/30/M/ST9/00757 and by the Polish Ministry of Science and Higher Education grant DIR/WK/2018/12.

ORCID iDs

Maria G. Dainotti  <https://orcid.org/0000-0003-4442-8546>
 Ritwik Sharma  <https://orcid.org/0000-0003-1858-473X>
 Aditya Narendra  <https://orcid.org/0000-0003-1265-2981>
 Delina Levine  <https://orcid.org/0000-0003-3411-6370>
 Enrico Rinaldi  <https://orcid.org/0000-0003-4134-809X>
 Agnieszka Pollo  <https://orcid.org/0000-0003-3358-0665>
 Gopal Bhatta  <https://orcid.org/0000-0002-0705-6619>

References

Ahumada, T., Singer, L. P., Anand, S., et al. 2021, *NatAs*, 5, 917
 Aloy, M. Á., & Obergaulinger, M. 2021, *MNRAS*, 500, 4365
 Barthelmy, S. D., Barbier, L. M., Cummings, J. R., et al. 2005, *SSRv*, 120, 143
 Beskin, G., Karpov, S., Bondar, S., et al. 2010, *ApJL*, 719, L10
 Bi, X., Mao, J., Liu, C., & Bai, J.-M. 2018, *ApJ*, 866, 97
 Blake, C. H., Bloom, J. S., Starr, D. L., et al. 2005, *Natur*, 435, 181
 Bloom, J. S., Kulkarni, S. R., & Djorgovski, S. G. 2002, *AJ*, 123, 1111
 Bucciantini, N., Metzger, B. D., Thompson, T. A., & Quataert, E. 2012, *MNRAS*, 419, 1537
 Bucciantini, N., Quataert, E., Arons, J., Metzger, B. D., & Thompson, T. A. 2008, *MNRAS*, 383, L25
 Burrows, D. N., Hill, J. E., Nousek, J. A., et al. 2005, *SSRv*, 120, 165
 Cano, Z., Wang, S.-Q., Dai, Z.-G., & Wu, X.-F. 2017, *AdAst*, 2017, 8929054
 Cao, S., Dainotti, M., & Ratra, B. 2022a, *MNRAS*, 512, 439
 Cao, S., Khadka, N., & Ratra, B. 2022b, *MNRAS*, 510, 2928
 Cardone, V. F., Capozziello, S., & Dainotti, M. G. 2009, *MNRAS*, 400, 775
 Cardone, V. F., Dainotti, M. G., Capozziello, S., & Willingale, R. 2010, *MNRAS*, 408, 1181
 Cavallo, G., & Rees, M. J. 1978, *MNRAS*, 183, 359

Encko, S. B., Frail, D. A., Harrison, F. A., et al. 2010, *ApJ*, 711, 641
 Chincarini, G., Mao, J., Margutti, R., et al. 2010, *MNRAS*, 406, 2113
 Conley, A., Guy, J., Sullivan, M., et al. 2011, *ApJS*, 192, 1
 Costa, E., Frontera, F., Heise, J., et al. 1997, *Natur*, 387, 783
 Cucchiara, A., Levan, A. J., Fox, D. B., et al. 2011, *ApJ*, 736, 7
 Dainotti, M., Levine, D., Fraija, N., et al. 2023a, *Galax*, 11, 25
 Dainotti, M. G., Bernardini, M. G., Bianco, C. L., et al. 2007, *A&A*, 471, L29
 Dainotti, M. G., Cardone, V. F., & Capozziello, S. 2008, *MNRAS*, 391, L79
 Dainotti, M. G., De Simone, B., Islam, K. M., et al. 2022a, *ApJ*, 938, 41
 Dainotti, M. G., De Simone, B., Schiavone, T., et al. 2021a, *ApJ*, 912, 150
 Dainotti, M. G., Del Vecchio, R., Shigehiro, N., & Capozziello, S. 2015, *ApJ*, 800, 31
 Dainotti, M. G., Fabrizio Cardone, V., Capozziello, S., Ostrowski, M., & Willingale, R. 2011, *ApJ*, 730, 135
 Dainotti, M. G., Lenart, A. L., Chraya, A., et al. 2022b, *MNRAS*, 518, 2201
 Dainotti, M. G., Lenart, A. L., Chraya, A., et al. 2023b, *MNRAS*, 518, 2201
 Dainotti, M. G., Lenart, A. L., Fraija, N., et al. 2021b, *PASJ*, 73, 970
 Dainotti, M. G., Lenart, A. L., Sarracino, G., et al. 2020a, *ApJ*, 904, 97
 Dainotti, M. G., Levine, D., Fraija, N., Warren, D., & Sourav, S. 2022c, *ApJ*, 940, 169
 Dainotti, M. G., Livermore, S., Kann, D. A., et al. 2020b, *ApJL*, 905, L26
 Dainotti, M. G., Nagataki, S., Maeda, K., Postnikov, S., & Pian, E. 2017, *A&A*, 600, A98
 Dainotti, M. G., Nielson, V., Sarracino, G., et al. 2022d, *MNRAS*, 514, 1828
 Dainotti, M. G., Omodei, N., Srinivasaragavan, G. P., et al. 2021d, *ApJS*, 255, 13
 Dainotti, M. G., Petrosian, V., Singal, J., & Ostrowski, M. 2013, *ApJ*, 774, 157
 Dainotti, M. G., Postnikov, S., Hernandez, X., & Ostrowski, M. 2016, *ApJL*, 825, L20
 Dainotti, M. G., Sarracino, G., & Capozziello, S. 2022e, *PASJ*, 74, 1095
 Dainotti, M. G., Singal, J., Ostrowski, M., et al. 2013, *ApJ*, 774, 157
 Dainotti, M. G., Willingale, R., Capozziello, S., Fabrizio Cardone, V., & Ostrowski, M. 2010, *ApJL*, 722, L215
 Dainotti, M. G., Young, S., Li, L., et al. 2022f, *ApJS*, 261, 25
 De Pasquale, M., Evans, P., Oates, S., et al. 2008, *MNRAS*, 392, 153
 Dichiaro, S., Troja, E., Beniamini, P., et al. 2021, *ApJL*, 911, L28
 Duncan, R. C., & Thompson, C. 1992, *ApJL*, 392, L9
 Evans, P. A., Beardmore, A. P., Page, K. L., et al. 2007, *A&A*, 469, 379
 Evans, P. A., Beardmore, A. P., Page, K. L., et al. 2009, *MNRAS*, 397, 1177
 Fraija, N., Laskar, T., Dichiaro, S., et al. 2020, *ApJ*, 905, 112
 Gao, H., Lei, W.-H., Zou, Y.-C., Wu, X.-F., & Zhang, B. 2013, *NewAR*, 57, 141
 Gehrels, N., Chincarini, G., Giommi, P., et al. 2004, *ApJ*, 611, 1005
 Gehrels, N., Ramirez-Ruiz, E., & Fox, D. B. 2009, *ARA&A*, 47, 567
 Geiger, B., & Schneider, P. 1996, *MNRAS*, 282, 530
 Gendre, B., Joyce, Q. T., Orange, N. B., et al. 2019, *MNRAS*, 486, 2471
 Gendre, B., Stratta, G., Atteia, J. L., et al. 2013, *ApJ*, 766, 30
 Giblin, T. W., Connaughton, V., van Paradijs, J., et al. 2002, *ApJ*, 570, 573
 Gorbovskoy, E. S., Lipunova, G. V., Lipunov, V. M., et al. 2012, *MNRAS*, 421, 1874
 Greiner, J., Mazzali, P. A., Kann, D. A., et al. 2015, *Natur*, 523, 189
 Hjorth, J., & Bloom, J. S. 2012, in *Gamma-Ray Bursts*, ed. C. Kouveliotou et al. (Cambridge: Cambridge Univ. Press)
 Hjorth, J., Sollerman, J., Møller, P., et al. 2003, *Natur*, 423, 847
 Huber, K., Czesla, S., Wolter, U., & Schmitt, J. 2010, *A&A*, 514, A39
 Kann, D. A., Klose, S., & Zeh, A. 2006, *ApJ*, 641, 993
 Kann, D. A., Klose, S., Zhang, B., et al. 2010, *ApJ*, 720, 1513
 Kann, D. A., Klose, S., Zhang, B., et al. 2011, *ApJ*, 734, 96
 Kann, D. A., Schady, P., Olivares, E. F., et al. 2018, *A&A*, 617, A122
 Kouveliotou, C., Meegan, C. A., Fishman, G. J., et al. 1993, *ApJL*, 413, L101
 Kumar, P., & Barniol Duran, R. 2010, *MNRAS*, 409, 226
 Kumar, P., Narayan, R., & Johnson, J. L. 2008, *Sci*, 321, 376
 Levan, A. J., Jakobsson, P., Hurkett, C., et al. 2007, *MNRAS*, 378, 1439
 Levan, A. J., Tanvir, N. R., Jakobsson, P., et al. 2008, *MNRAS*, 384, 541
 Levan, A. J., Tanvir, N. R., Starling, R. L. C., et al. 2014, *ApJ*, 781, 13
 Levesque, E. M., Bloom, J. S., Butler, N. R., et al. 2010, *MNRAS*, 401, 963
 Levine, D., Dainotti, M., Fraija, N., et al. 2023, *MNRAS*, 519, 4670
 Li, L., Liang, E.-W., Tang, Q.-W., et al. 2012, *ApJ*, 758, 27
 Li, L., Wang, Y., Shao, L., et al. 2018a, *ApJS*, 234, 26
 Li, L., Wu, X.-F., Huang, Y.-F., et al. 2015, *ApJ*, 805, 13
 Li, L., Wu, X.-F., Lei, W.-H., et al. 2018b, *ApJS*, 236, 26
 Liang, E.-W., Lü, H.-J., Hou, S.-J., Zhang, B.-B., & Zhang, B. 2009, *ApJ*, 707, 328
 Liang, E.-W., Zhang, B.-B., & Zhang, B. 2007, *ApJ*, 670, 565
 Lien, A., Sakamoto, T., Barthelmy, S. D., et al. 2016, *ApJ*, 829, 7
 Lipunov, V., Kornilov, V., Gorbovskoy, E., et al. 2018, *ATel*, 11429, 1

- Lyman, J. D., Levan, A. J., Tanvir, N. R., et al. 2017, *MNRAS*, **467**, 1795
- MacFadyen, A. I., & Woosley, S. E. 1999, *ApJ*, **524**, 262
- Margutti, R., Zaninoni, E., Bernardini, M. G., et al. 2013, *MNRAS*, **428**, 729
- Mazets, E., Golenetskii, S., Il'Inskii, V., et al. 1981, *Ap&SS*, **80**, 3
- Melandri, A., Covino, S., Rogantini, D., et al. 2014, *A&A*, **565**, A72
- Mészáros, P. 1997, *RvMA*, **10**, 127
- Mészáros, P. 2001, *PTbPS*, **143**, 33
- Mészáros, P., & Rees, M. J. 1993, *ApJ*, **405**, 278
- Metzger, B. D., Giannios, D., Thompson, T. A., Bucciantini, N., & Quataert, E. 2011, *MNRAS*, **413**, 2031
- Misra, K., Resmi, L., Kann, D. A., et al. 2021, *MNRAS*, **504**, 5685
- Nakauchi, D., Kashiyama, K., Suwa, Y., & Nakamura, T. 2013, *ApJ*, **778**, 67
- Narayan, R., Paczynski, B., & Piran, T. 1992, *ApJL*, **395**, L83
- Newville, M., Stensitzki, T., Allen, D. B., et al. 2016, Lmfit: Non-Linear Least-Square Minimization and Curve-Fitting for Python, Astrophysics Source Code Library, ascl:1606.014
- Ngeow, C.-C., Kanbur, S. M., Nikolaev, S., Tanvir, N. R., & Hendry, M. A. 2003, *ApJ*, **586**, 959
- Norris, J. P., & Bonnell, J. T. 2006, *ApJ*, **643**, 266
- Norris, J. P., Gehrels, N., & Scargle, J. D. 2010, *ApJ*, **717**, 411
- Norris, J. P., Marani, G. F., & Bonnell, J. T. 2000, *ApJ*, **534**, 248
- Nousek, J. A., Kouveliotou, C., Grupe, D., et al. 2006, *ApJ*, **642**, 389
- Oates, S. R., Page, M. J., De Pasquale, M., et al. 2012, *MNRAS*, **426**, L86
- O'Brien, P. T., Willingale, R., Osborne, J., et al. 2006, *ApJ*, **647**, 1213
- Paczynski, B. 1998, *ApJL*, **494**, L45
- Panaitescu, A., & Kumar, P. 2000, *ApJ*, **543**, 66
- Panaitescu, A., & Kumar, P. 2001, *ApJL*, **560**, L49
- Panaitescu, A., & Vestrand, W. T. 2008, *MNRAS*, **387**, 497
- Panaitescu, A., & Vestrand, W. T. 2011, *MNRAS*, **414**, 3537
- Perna, R., Lazzati, D., & Cantiello, M. 2018, *ApJ*, **859**, 48
- Perna, R., Lazzati, D., & Giacomazzo, B. 2016, *ApJL*, **821**, L18
- Piran, T. 1999, *PhR*, **314**, 575
- Piran, T. 2004, *RvMP*, **76**, 1143
- Piro, L., Amati, L., Antonelli, L. A., et al. 1998, *A&A*, **331**, L41
- Piro, L., Troja, E., Gendre, B., et al. 2014, *ApJL*, **790**, L15
- Postnikov, S., Dainotti, M. G., Hernandez, X., & Capozziello, S. 2014, *ApJ*, **783**, 126
- Racusin, J. L., Liang, E. W., Burrows, D. N., et al. 2009, *ApJ*, **698**, 43
- Roming, P. W. A., Kennedy, T. E., Mason, K. O., et al. 2005, *SSRv*, **120**, 95
- Rossi, A., Rothberg, B., Palazzi, E., et al. 2022, *ApJ*, **932**, 1
- Rowlinson, A., Gompertz, B. P., Dainotti, M., et al. 2014, *MNRAS*, **443**, 1779
- Ryan, G., van Eerten, H., Piro, L., & Troja, E. 2020, *ApJ*, **896**, 166
- Sakamoto, T., Barthelmy, S. D., Barbier, L., et al. 2008, *ApJS*, **175**, 179
- Sakamoto, T., Barthelmy, S. D., Baumgartner, W. H., et al. 2011, *ApJS*, **195**, 2
- Sakamoto, T., Hill, J. E., Yamazaki, R., et al. 2007, *ApJ*, **669**, 1115
- Salvaterra, R., Della Valle, M., Campana, S., et al. 2009, *Natur*, **461**, 1258
- Scargle, J. D. 2020, *ApJ*, **895**, 90
- Si, S.-K., Qi, Y.-Q., Xue, F.-X., et al. 2018, *ApJ*, **863**, 50
- Soderberg, A. M., Kulkarni, S. R., Berger, E., et al. 2004, *ApJ*, **606**, 994
- Srinivasaragavan, G. P., Dainotti, M. G., Fraija, N., et al. 2020, *ApJ*, **903**, 18
- Stratta, G., Dainotti, M. G., Dall'Osso, S., Hernandez, X., & De Cesare, G. 2018, *ApJ*, **869**, 155
- Stratta, G., Gendre, B., Atteia, J. L., et al. 2013, *ApJ*, **779**, 66
- Tagliaferri, G., Goad, M., Chincarini, G., et al. 2005, *Natur*, **436**, 985
- Tak, D., Omodei, N., Uhm, Z. L., et al. 2019, *ApJ*, **883**, 134
- Tanvir, N. R., Fox, D. B., Levan, A. J., et al. 2009, *Natur*, **461**, 1254
- Thompson, C. 1994, *MNRAS*, **270**, 480
- Tian, J., Anderson, G. E., Hancock, P. J., et al. 2022, *PASA*, **39**, e003
- Troja, E., Cusumano, G., O'Brien, P. T., et al. 2007, *ApJ*, **665**, 599
- Usov, V. V. 1992, *Natur*, **357**, 472
- van Paradijs, J., Groot, P. J., Galama, T., et al. 1997, *Natur*, **386**, 686
- van Putten, M. H. P. M., Lee, G. M., Della Valle, M., Amati, L., & Levinson, A. 2014, *MNRAS*, **444**, L58
- Vestrand, W. T., Wozniak, P. R., Wren, J. A., et al. 2005, *Natur*, **435**, 178
- Vestrand, W. T., Wren, J. A., Panaitescu, A., et al. 2014, *Sci*, **343**, 38
- Wang, X.-G., Zhang, B., Liang, E.-W., et al. 2015, *ApJS*, **219**, 9
- Willingale, R., O'Brien, P. T., Osborne, J. P., et al. 2007, *ApJ*, **662**, 1093
- Woosley, S. E. 1993, *ApJ*, **405**, 273
- Woosley, S. E., & Bloom, J. S. 2006, *ARA&A*, **44**, 507
- Woosley, S. E., & Heger, A. 2006, *ApJ*, **637**, 914
- Xu, M., & Tang, Q. W. 2021, *ApJ*, **911**, 76
- Yi, S.-X., Xi, S.-Q., Yu, H., et al. 2016, *ApJS*, **224**, 20
- Zaninoni, E., Bernardini, M. G., Margutti, R., Oates, S., & Chincarini, G. 2013, *A&A*, **557**, A12
- Zeh, A., Kloke, S., & Kann, D. A. 2006, *ApJ*, **637**, 889
- Zhang, B., Fan, Y. Z., Dyks, J., et al. 2006, *ApJ*, **642**, 354
- Zhang, B., Liang, E., Page, K. L., et al. 2007b, *ApJ*, **655**, 989
- Zhang, B., & Mészáros, P. 2002, *ApJ*, **581**, 1236
- Zhang, B., & Mészáros, P. 2004, *IJMPA*, **19**, 2385
- Zhang, B., Zhang, B.-B., Liang, E.-W., et al. 2007a, *ApJL*, **655**, L25
- Zhang, B., Zhang, B.-B., Virgili, F. J., et al. 2009, *ApJ*, **703**, 1696
- Zhang, B. B., Liu, Z. K., Peng, Z. K., et al. 2021, *NatAs*, **5**, 911
- Zhang, B.-B., Zhang, B., Murase, K., Connaughton, V., & Briggs, M. S. 2014, *ApJ*, **787**, 66